

Physics-informed neural network for fatigue life prediction of irradiated austenitic and ferritic/martensitic steels

Dhiraj S. Kori¹, Abhinav Chandraker¹, Syed Abdur Rahman², Punit Rathore³, and Ankur Chauhan¹

¹Extreme Environments Materials Group, Department of Materials Engineering, Indian Institute of Science (IISc), Bengaluru, 560012 Karnataka, India

²Department of Materials, University of Oxford, Parks Road, Oxford, OX1 3PH, United Kingdom

³Robert Bosch Centre for Cyberphysical Systems, Indian Institute of Science (IISc), Bengaluru, 560012 Karnataka, India

*Corresponding author: ankurchauhan@iisc.ac.in

Abstract

This study proposes a Physics-Informed Neural Network (PINN) framework to predict the low-cycle fatigue (LCF) life of irradiated austenitic and ferritic/martensitic (F/M) steels used in nuclear reactors. These materials experience cyclic loading and irradiation at elevated temperatures, causing complex degradation that traditional empirical models fail to capture accurately. The developed PINN model incorporates physical fatigue life constraints into its loss function, improving prediction accuracy and generalizability. Trained on 495 data points, including both irradiated and unirradiated conditions, the model outperforms traditional machine learning models like Random Forest, Gradient Boosting, eXtreme Gradient Boosting, and the conventional Neural Network. SHapley Additive exPlanations analysis identifies strain amplitude, irradiation dose, and testing temperature as dominant features, each inversely correlated with fatigue life, consistent with physical understanding. PINN captures saturation behaviour in fatigue life at higher strain amplitudes in F/M steels. Overall, the PINN framework offers a reliable and interpretable approach for predicting fatigue life in irradiated alloys, enabling informed alloy selection.

Keywords: Irradiated stainless steels; Fatigue life prediction; Machine learning; Physical constraints; Neural networks

1. Introduction

As nuclear energy gains traction as a low-emission power source, ensuring the durability of both fusion and fission reactors components under high temperatures, irradiation, and cyclic loading becomes critical. Fatigue failures, often sudden and below fracture limits, pose a key challenge to reactor reliability [1]. Under irradiation, atoms are displaced from lattice sites, forming point defects that develop into dislocation loops, voids, segregation, and precipitates [2]. These microstructural changes severely degrade material properties, causing irradiation hardening, embrittlement, and significantly reducing fatigue life [3].

Austenitic and F/M steels are widely used in nuclear reactors for their complementary properties. Austenitic steels offer corrosion resistance, durability, and efficient heat transfer, with good creep resistance from their FCC structure, though high thermal expansion can impair fatigue performance [1]. F/M steels, having a BCC lattice, offer lower creep resistance but superior fatigue behaviour, higher thermal conductivity, and strong resistance to irradiation-induced swelling, making them ideal for advanced reactors [4].

Reactor components face fatigue degradation despite materials' favourable properties due to constraint cyclic stresses, vibrations, and temperature changes [1]. Specifically, fusion tokamaks like ITER and DEMO operate cyclically and face plasma instabilities such as Multifaceted Asymmetric Radiation From the Edges (MARFEs) [5,6], while fission reactor cores too undergo cyclic thermal and neutron-irradiation loads that drive thermomechanical fatigue and set structural component lifetimes [7]. Therefore, accurately predicting fatigue life under such conditions, therefore, becomes vital but is challenging. Traditional numerical approaches, such as those based on the Chaboche's viscoplasticity model and continuum damage mechanics, have been applied to both irradiated [8] and nonirradiated steels [9–11]. While effective, these models are computationally intensive and require extensive parameter calibration, which depends on multiple low-cycle fatigue (LCF) datasets across temperatures—a major limitation when working with irradiated specimens. An alternative strategy involves estimating parameters for the Manson, Coffin, and Basquin empirical equations [12–14] using tensile properties. This method has been applied to predict the fatigue life of non-irradiated F/M steels in both air and vacuum [15–17]. However, these empirical models also rely on costly, large-scale testing and often fall short in capturing the complex interplay of variables such as alloy composition, temperature, coolant environment, and irradiation effects.

In the era of big data and high-performance computing, machine learning (ML) employs advanced algorithms to construct predictive models and rigorously quantify the uncertainties in their forecasts [18–20]. By efficiently mapping complex input features to target outputs, ML offers a compelling alternative to traditional fatigue-life models [21–27] and has proven effective in predicting various forms of irradiation-induced material degradation [28]. For instance, different ML algorithms have been employed to model irradiation hardening in low-activation steels [29,30], while Cubist, eXtreme Gradient Boosting (XGB), and Support Vector Machine have been used to predict the ductile-to-brittle transition temperature of neutron-irradiated reactor pressure vessel steels [31] [32]. Linear Regression (LR), Gradient Boosting (GB), and Artificial Neural Networks (ANNs) have also been shown to estimate void swelling [33], while the XGB and ANN have been employed to predict irradiation creep [34] in steels. However, usage of ML for predicting the fatigue life of irradiated steels is very limited. Zahran et. al. [35,36] recently implemented a data-driven ML framework—using Random Forest, Support Vector Regressor (SVR), Gradient Boosted Regressor (GBR), and Multi-Layer Perceptron (MLP)—to forecast the LCF life of both unirradiated and neutron-irradiated reduced-activation F/M steels.

Applications to other structural alloys, notably irradiated austenitic steels, remain scarce due to the high cost and long lead times of irradiation fatigue testing [37]. Additionally, conventional ML models trained on limited data exhibit poor generalization beyond the training domain. To overcome this, Physics-informed Neural Networks (PINNs) address this by embedding physical knowledge into the model, enhancing accuracy, convergence, and robustness, especially with scarce data [38] [39]. For instance, Zhang et al. [40] predicted the creep-fatigue life of 316 stainless steel using PINNs, while Chen et al. [41] incorporated probabilistic fatigue behaviour for better interpretability. Advances include hybrid loss functions with physical constraints [42] [43] [44], fracture mechanics-based fatigue prediction in additive materials [45], and multiaxial fatigue constraints within generative adversarial networks [46].

Building on these advances, we develop a PINN model to predict the LCF life of unirradiated and irradiated austenitic and F/M steels, incorporating strain amplitude, temperature, and irradiation fluence as physical variables. By embedding physical constraints like fatigue-related partial derivatives with respect to these variables into the loss function, the model

delivers physically consistent, more accurate predictions, outperforming conventional ML models.

2. Methodology

Fully reversed ($R = -1$) strain-controlled LCF data for various austenitic steels (AISI SS310, SS304, SS304L, SS316, SS316L) and F/M steels (HT9, T91, F82H, OPTIFER, and EUROFER97) were compiled from the literature [47–58]. The data comprises 495 data points, which include 254 unirradiated and 241 irradiated specimens.

For model development, the data was split into training and testing subsets. The training allowed the ML models to learn underlying patterns, while the testing evaluated their predictive performance unbiasedly. Model performance can vary with different data splits. To ensure robustness, the “random_state” parameter was varied, training and testing the model across six combinations (two train-test ratios: 80:20 and 70:30, each with three random states). This confirmed the model’s generalizability beyond a single split.

The model was trained over 50 input features, including elemental composition of the steels in wt. % (see Table S.1 in the Supplementary Materials), pre-irradiation treatment parameters such as temperature ($^{\circ}\text{C}$), time (min), for processing conditions such as cold-working, hot rolling, cold-swaging, normalizing, annealing, tempering, irradiation parameters including radiation dose (dpa), irradiation temperature ($^{\circ}\text{C}$) and irradiation environments such as Helium, Neon, Argon, Static/flowing Sodium and the absence of an environment/air; testing parameters such as strain amplitude (%), test temperature ($^{\circ}\text{C}$), strain rate (s^{-1}); and specimen type (cylindrical or hourglass) and their respective dimensions (mm). Most of the utilized irradiated data is collected in Static Sodium Environment (39%), followed by the absence of an environment/air (25%), Argon (20%), flowing Sodium (10%), and lastly by Helium-Neon (6%). The range of values for the input features is provided in Table S.2 in the Supplementary Materials.

Categorical or non-numerical input features like irradiation environment and pre-treatment were one-hot encoded, converting each category into binary variables (1 for presence, 0 for absence) to capture their influence [59]. Processing treatments with available temperature and time data, i.e., annealing, hot rolling, normalizing, tempering, were treated as separate features.

Others lacking detailed parameters, such as solution-annealing, hot-then-cold-swaging, cold-working, chill-swaged-tempering, were one-hot encoded due to limited data.

To ensure consistency and improve ML models' performance, all input features were normalized using:

$$x_{\text{norm}} = \frac{x - x_{\text{min}}}{x_{\text{max}} - x_{\text{min}}} \quad (1)$$

where x is the input feature, and x_{min} and x_{max} are its minimum and maximum values, respectively. Normalization scales features to a 0–1 range, removing dimensional disparities, enhancing model stability, and promoting faster convergence. Missing (NaN) and infinite values (the feature radius of curvature being infinite corresponding to a cylindrical sample) were replaced with -10 and 10 , respectively, to minimize their influence on learning.

Radiation dosage (dpa) was used instead of fluence to simplify interpretation and improve accuracy, as neutron fluence spans a wide range up to $1.01 \times 10^{23} \text{ n/cm}^2$ or 71 dpa. A fluence of 10^{22} n/cm^2 corresponds to ~ 7 dpa for $E \geq 0.1 \text{ MeV}$ [60]. Dosage values were computed accordingly. The output variable, fatigue life (N), was logarithmically scaled to reduce variability and improve prediction accuracy.

Inspired by Raissi et al. [61] and Jiang et al. [62], a PINN architecture (Fig. 1) was developed by embedding a physics-informed loss function into the neural network. The partial derivatives of fatigue life with respect to test parameters, i.e., strain amplitude (ϵ), temperature (T), and radiation dosage (d), represent the sensitivity of fatigue behavior to these conditions. These are incorporated as inequality constraints ($\frac{\partial N}{\partial \epsilon} \leq 0$, $\frac{\partial^2 N}{\partial \epsilon^2} \geq 0$, $\frac{\partial N}{\partial T} \leq 0$, $\frac{\partial N}{\partial d} \leq 0$) during training to enforce physically consistent learning.

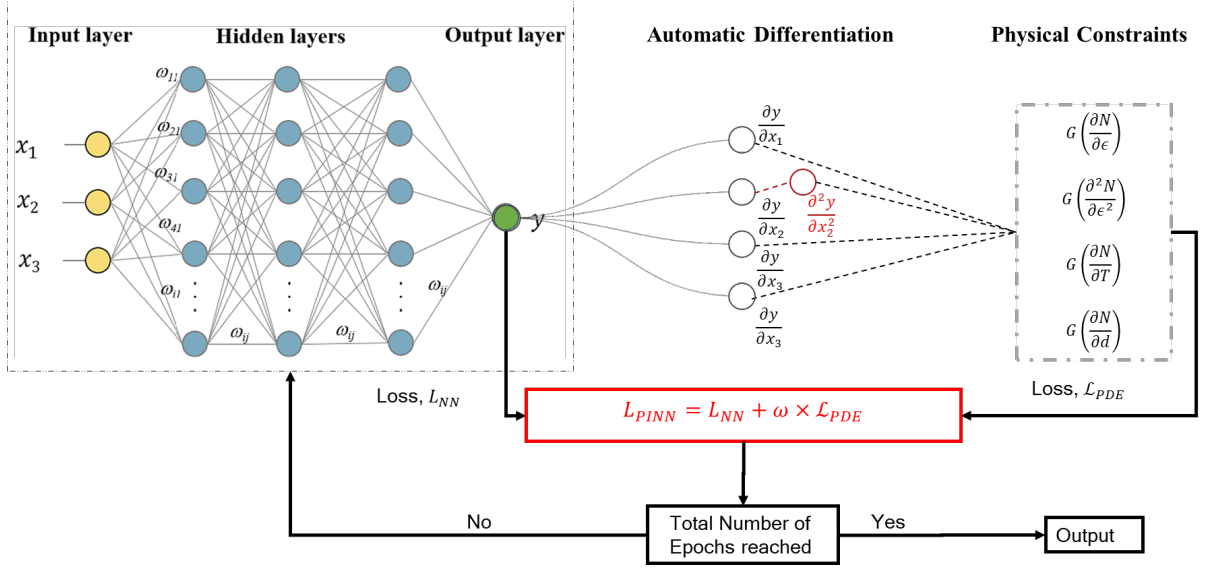


Fig. 1. The architecture of the PINN model consists of input, hidden, and output layers of NN, along with physical constraints.

PyTorch's automatic differentiation is used to compute these derivatives for each input feature, which works as follows:

$$\frac{\partial y}{\partial x_i} = \frac{\partial y}{\partial z_m^{(k)}} \sum_n \frac{\partial z_m^{(k)}}{\partial a_n^{(k-1)}} \frac{\partial a_n^{(k-1)}}{\partial z_n^{(k-1)}} \cdots \sum_p \frac{\partial z_r^{(3)}}{\partial a_p^{(2)}} \frac{\partial a_p^{(2)}}{\partial z_p^{(2)}} \sum_q \frac{\partial z_p^{(2)}}{\partial a_q^{(1)}} \frac{\partial a_q^{(1)}}{\partial z_q^{(1)}} \frac{\partial z_q^{(1)}}{\partial x_i} \quad (2)$$

$$\frac{\partial^2 y}{\partial x_i^2} = \left[\frac{\partial y}{\partial z_m^{(k)}} \right]' \sum_n \frac{\partial z_m^{(k)}}{\partial a_n^{(k-1)}} \frac{\partial a_n^{(k-1)}}{\partial z_n^{(k-1)}} \cdots \sum_p \frac{\partial z_r^{(3)}}{\partial a_p^{(2)}} \frac{\partial a_p^{(2)}}{\partial z_p^{(2)}} \sum_q \frac{\partial z_p^{(2)}}{\partial a_q^{(1)}} \frac{\partial a_q^{(1)}}{\partial z_q^{(1)}} \frac{\partial z_q^{(1)}}{\partial x_i}$$

$$+ \frac{\partial y}{\partial z_m^{(k)}} \left[\sum_n \frac{\partial z_m^{(k)}}{\partial a_n^{(k-1)}} \frac{\partial a_n^{(k-1)}}{\partial z_n^{(k-1)}} \cdots \sum_p \frac{\partial z_r^{(3)}}{\partial a_p^{(2)}} \frac{\partial a_p^{(2)}}{\partial z_p^{(2)}} \sum_q \frac{\partial z_p^{(2)}}{\partial a_q^{(1)}} \frac{\partial a_q^{(1)}}{\partial z_q^{(1)}} \frac{\partial z_q^{(1)}}{\partial x_i} \right]'$$

In this framework:

- **Input features** are denoted by x and represent the raw variables fed into the network.
- **Pre-activation**, denoted by z , refers to the weighted sum of inputs to a neuron—calculated before applying any activation function.
- **Activation**, denoted by a , is the neuron's output after applying the activation function to z .
- The **final output** of the network is represented by y , which corresponds to the network's prediction.

To distinguish between neurons and layers:

- **Subscripts** index neurons within a layer:
 - i for input features
 - q for neurons in the first hidden layer (layer 2)
 - p for neurons in the second hidden layer (layer 3)
 - m for neurons in the output layer (layer k)
- **Superscripts** indicate the layer number:
 - Layer 1 \rightarrow input features
 - Layer 2 \rightarrow first hidden layer
 - Layer $k \rightarrow$ final/output layer

For a detailed derivation, refer to Supplementary Material Section S.7.

The function, denoted as $G(x)$, transforms the derivatives within the loss function by scaling them to a range between 0 and 1. This non-linear transformation helps bind the derivatives, improving the stability and convergence of the optimization process. It integrates seamlessly into the loss function and is defined as:

$$G(x) = \frac{x}{1 + e^{\beta|x|}} \quad (3)$$

Where x is the input derivative value, and β controls the shape and steepness of the activation function and the influence of the physics-informed loss during training. For this model, β was set to 100, following Jiang et al. [62], as it yielded optimal results (See Supplementary Materials Section S.6 and Figure S.7 for further analysis).

To effectively integrate physics-based constraints into the neural network training, a custom loss function was developed by integrating both data-driven and physics-informed components. The total loss function is expressed as:

$$\mathcal{L}(y_{\text{true}}, y_{\text{pred}}) = H(y_{\text{true}}, y_{\text{pred}}) + R \quad (4)$$

Here, H denotes the Huber loss, which calculates the loss between predicted (y_{pred}) and actual (y_{true}) fatigue life values [63]. It integrates squared error and absolute error terms to prevent overfitting and improve robustness to outliers. It smoothly transitions between squared and absolute error regimes based on a threshold parameter δ . It is defined as:

$$H(y_{\text{true}}, y_{\text{pred}}) = \begin{cases} \frac{1}{2}(y_{\text{true}} - y_{\text{pred}})^2, & \text{if } |y_{\text{true}} - y_{\text{pred}}| \leq \delta \\ \delta \left(|y_{\text{true}} - y_{\text{pred}}| - \frac{\delta}{2} \right), & \text{otherwise} \end{cases} \quad (5)$$

In this study, $\delta = 1$ was selected to define the transition point between the quadratic and linear regimes.

A regularization term R was added to penalize excessive deviation of predictions from their means, to regulate model complexity further and improve generalization. This term discourages overfitting to noisy data and smoothens the learned function. It is given by:

$$R = q \left(\frac{1}{n} \sum_{i=1}^n y_{\text{pred},i} \right)^2 \quad (6)$$

where $y_{\text{pred},i}$ is the predicted output for the i^{th} sample, n is the number of samples, and q is a weighting factor (set to 0.01) that controls the influence of the regularization term in the loss function.

The final physics-derived loss, Loss_{PDE} , enforces known fatigue behavior through constraints on the partial derivatives of the predicted fatigue life N with respect to relevant test parameters: ϵ , T , and d . Each derivative is first transformed via a sigmoid-like function $G(x)$ to bound its value between 0 and 1. Then, the physics-informed loss is computed as:

$$\begin{aligned} \text{Loss}_{\text{PDE}} = & \mathcal{L} \left(0, G_{\text{out}} \left(\frac{\partial N}{\partial \epsilon} \right) \right) + \mathcal{L} \left(0, G_{\text{out}} \left(\frac{\partial^2 N}{\partial \epsilon^2} \right) \right) + \mathcal{L} \left(0, G_{\text{out}} \left(\frac{\partial N}{\partial T} \right) \right) \\ & + \mathcal{L} \left(0, G_{\text{out}} \left(\frac{\partial N}{\partial d} \right) \right) \end{aligned} \quad (7)$$

where G_{out} denotes the transformed derivative, $\mathcal{L}(0, \dots)$ uses the same combined Huber + regularization form from Equation (4), with a zero “true” target to enforce constraints. By construction, these terms drive the network to satisfy: $\frac{\partial N}{\partial \epsilon} \leq 0$, $\frac{\partial^2 N}{\partial \epsilon^2} \geq 0$, $\frac{\partial N}{\partial T} \leq 0$, $\frac{\partial N}{\partial d} \leq 0$. ensuring that fatigue life decreases (or at least does not increase) as strain amplitude, temperature, or dosage increases, and its curvature in strain amplitude is non-negative.

Finally, the total PINN loss is defined by combining the standard neural network loss, $\text{Loss}_{\text{PINN}}$, with the physics-derived term:

$$\text{LOSS}_{\text{PINN}} = \text{LOSS}_{\text{NN}} + \omega \times \text{LOSS}_{\text{PDE}} \quad (8)$$

The hyperparameter ω controls the relative weight of the physics-informed component: higher ω emphasizes adherence to physical constraints, while lower ω gives more freedom to fit data. By tuning ω , the model balances data fidelity and physically consistent predictions.

To enhance training stability and performance, Nakamura et al.'s [64] learning rate schedule was utilized, which combines a warmup phase with a sigmoid decay. In this approach, the learning rate increases linearly at the start (warmup phase) and then gradually decreases following a sigmoid function. This approach improves convergence and test accuracy.

To benchmark the PINN, we compared it with four data-driven ML models—Random Forest (RF), Gradient Boost (GB), eXtreme Gradient Boost (XGB), and a conventional Neural Network (NN)—trained to predict cycles to failure. These models and the utilized hyperparameters are described briefly in the Supplementary Materials, see Tables S.3 to S.7. Performance was evaluated using two standard metrics, the coefficient of determination (R^2) and Mean Squared Error (MSE), with hyperparameters optimized via Bayesian search for best accuracy and generalization.

To interpret model predictions and feature roles, SHapley Additive exPlanations (SHAP) analysis was utilized. Based on cooperative game theory, SHAP assigns each input feature a contribution value for a given prediction (see Supplementary Materials Section 2.2.5 for more details). These are visualized using summary plots, where each horizontal data point spread shows the overall impact of a feature across all samples.

Lastly, a univariate trend analysis assessed individual feature effects on fatigue life by varying radiation dose (dpa) across different strain amplitudes while keeping other inputs fixed. A synthetic dataset within the original training range was generated, and the trained PINN model predicted cycles to failure for these inputs.

3. Results and discussion

3.1. PINN training-testing and comparison with other ML models

Model performance was evaluated using an 80:20 training-to-testing data split generated from the third random state. The train and test R^2 and MSE for all five employed models, RF, GB, XGB, NN, and the proposed PINN, for this split and random state are listed in Tables S.8 to

S.11 in the Supplementary Materials. Additionally, Fig. 2 compares the predictive accuracy of the five models on the testing data (see similar comparison of the training data provided as Fig. S.4 in the Supplementary Materials). From Fig. 2, the PINN model demonstrated superior performance with the highest coefficient of determination ($R^2 = 0.879$) and the lowest mean squared error ($MSE = 0.059$). Notably, 99% of the PINN predictions fall within the ± 1 error band (Fig. 2e), indicating excellent agreement with experimental fatigue life data. In contrast, the other models showed a larger spread, with R^2 ranging from 0.849 to 0.866 and MSE between 0.066 and 0.075 (see Fig. 2). A small percentage of predictions from RF, GB, XGB, and NN exceeded the $\pm 2\%$ error margin, while PINN showed no such outliers, with clustering along the parity line and within the factor-of-2 bounds further highlights its robustness and improved generalization.

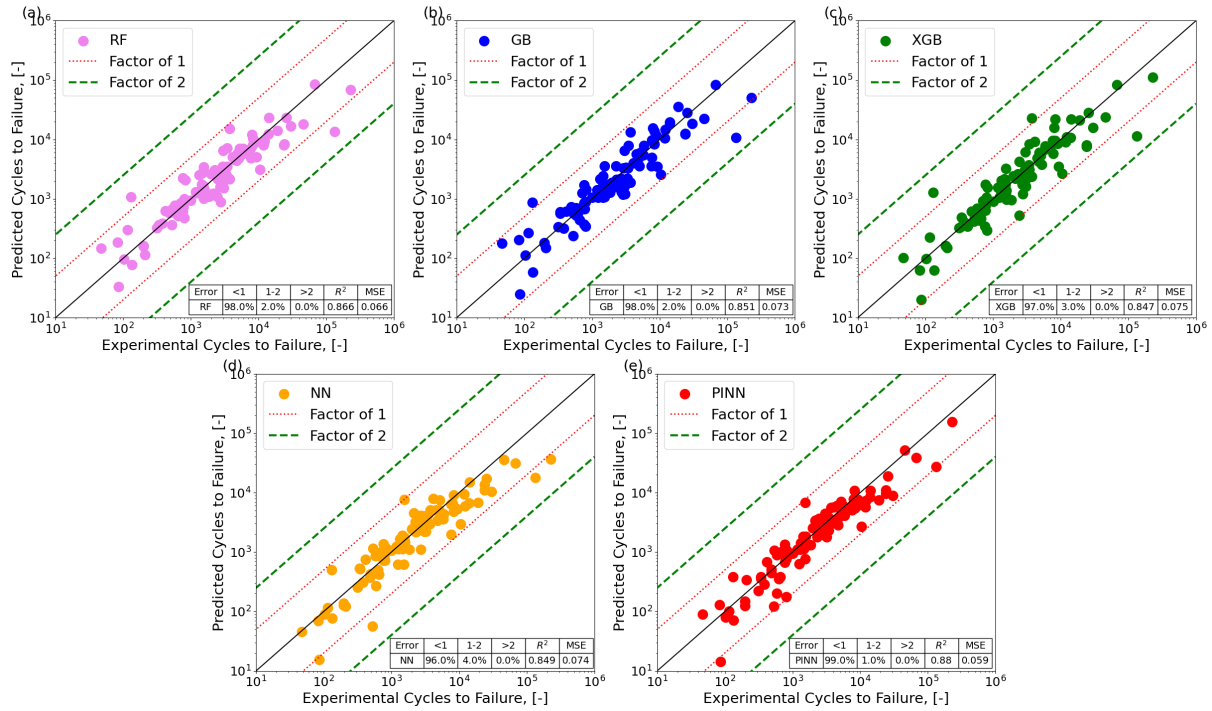


Fig. 2: Comparison of predicted vs. experimental fatigue life for the testing data using (a) RF, (b) GB, (c) XGB, (d) NN, and (e) PINN models. The red dotted lines indicate the ± 1 error band, and the green dashed lines denote the ± 2 error band. All model predictions fall within the ± 2 error band, with the PINN model exhibiting the highest accuracy and precision among the compared approaches.

To evaluate model robustness and sensitivity to data partitioning, the statistical variation in model performance across multiple random states was analyzed using R^2 and mean MSE, as illustrated in Fig. 3. While the proposed PINN model demonstrated strong performance in a representative case ($R^2 = 0.88$, $MSE = 0.059$, as discussed in Fig. 2e), its consistency across splits was particularly notable. Among all models, the PINN consistently yields the highest average R^2 (~ 0.85) with a narrow range of 0.82 to 0.88, and the lowest

average MSE (~ 0.07), ranging from 0.046 to 0.087, reflecting both high accuracy and robustness. In comparison, other models such as XGB, GB, RF, and NN showed relatively higher variability in performance than the PINN. The XGB model performed with moderate variance and good generalization and yielded R^2 values between 0.77 and 0.90, with MSE ranging from 0.034 to 0.111. The GB model followed closely, with R^2 ranging from 0.79 to 0.885 and MSE from 0.039 to 0.102. The RF model showed moderate accuracy, with R^2 between 0.797 and 0.894 and MSE ranging from 0.036 to 0.099. The NN model performed least consistently, with R^2 values between 0.75 and 0.87, and MSE between 0.043 and 0.125, indicating greater sensitivity to data partitioning. Overall, these findings highlight the advantage of embedding physics-informed constraints in neural networks, especially when dealing with limited or noisy data.

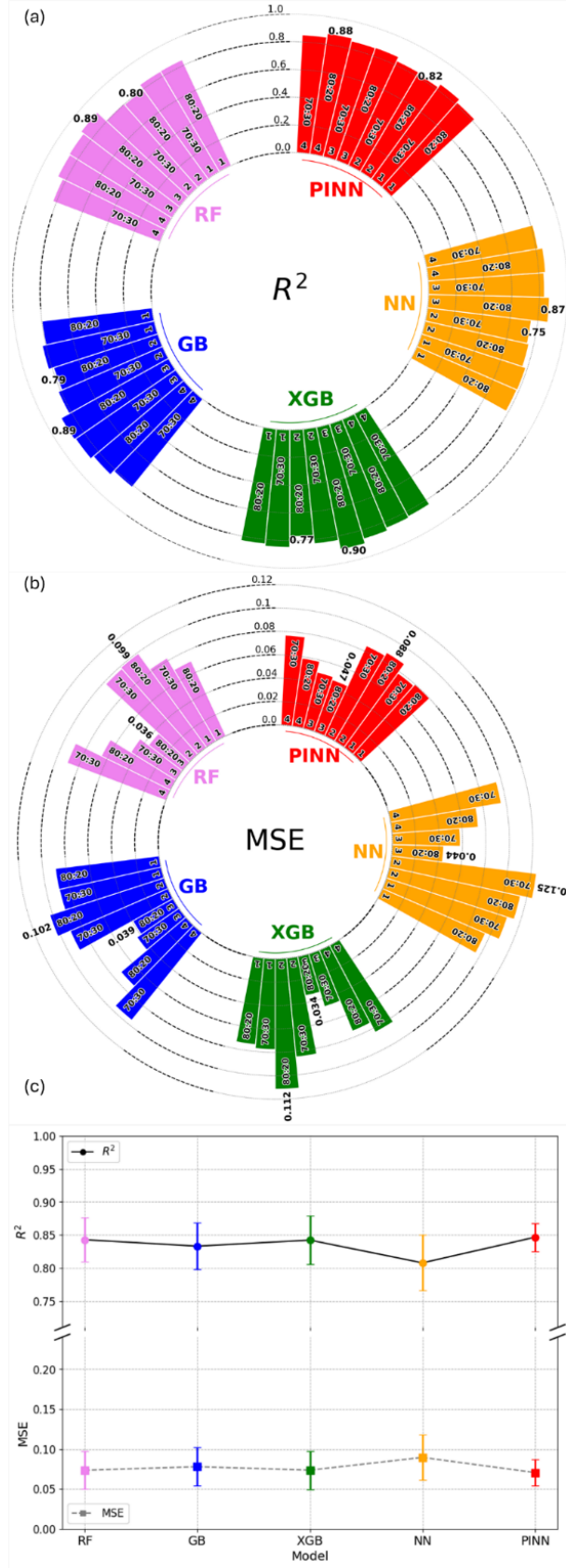


Fig. 3: (a) R^2 and (b) MSE for five predictive models, RF, GB, XGB, NN, and PINN, are presented. Each of the eight columns corresponds to a distinct combination of two train-test splits (70:30 and 80:20) across four different random states. (c) The average R^2 and MSE values across these combinations are shown with error bars representing the variance.

3.2. SHAP analysis – Input features' importance and their impact

Further insights into the interpretability of the PINN model were obtained through SHAP analysis, as illustrated in Fig. 4. As illustrated in Fig. 4, the SHAP plot highlights both the relative importance and the influence of each input feature on the model's output. Features are ranked vertically, with those contributing most to the model's performance appearing at the top. Each horizontal spread of coloured dots represents the impact of that feature across the data. Red dots on the right side of the vertical axis indicate that higher feature values contribute positively to the predicted LCF life, while blue dots suggest a negative correlation. This visualization allows classification of features into groups based on their directional impact.

The SHAP summary plot reveals that strain amplitude (%), test temperature (°C), and irradiation dosage (dpa) are the three most influential input features affecting the model's output—i.e., predicted LCF life. These features display predominantly negative SHAP values for higher feature magnitudes, indicating a negative/inverse relationship: increases in any of these parameters are associated with reducing the number of cycles to failure.

Among them, strain amplitude is the most dominant predictor. This also aligns well with work of Zahran et al [35]. At higher amplitudes, materials are subjected to larger cyclic stresses and strains [65], promoting intensified slip activity and more severe cyclic plastic deformation. This accelerates the development of three-dimensional dislocation substructures, such as dislocation walls, cells, and persistent slip bands, which serve as preferential sites for crack initiation [66,67], ultimately reducing fatigue life.

Test temperature is found to be the second essential key factor. Elevated temperatures reduce the shear modulus and enhance atomic diffusion, promoting dislocation motion through thermally activated mechanisms such as climb and cross-slip [68,69]. These mechanisms promote dynamic recovery and annihilation of dislocations, accelerating the formation and rearrangement of three-dimensional dislocation structures [68] and dislocations reaching the specimen surface. Thereby accelerating crack nucleation and propagation processes. Moreover, environmental effects such as oxidation further reduce fatigue resistance at high temperatures relative to specimens tested at ambient conditions [69,70].

The third influential factor, irradiation dosage, exerts a pronounced detrimental effect on fatigue life in the LCF regime. Higher irradiation levels promote the formation and

migration of defect clusters, such as interstitial/vacancy complexes, dislocation loops, and cavities [71]. While these defects generally act as obstacles for mobile dislocation, resulting in an irradiation-hardening, they simultaneously reduce the material's strain hardening capacity, lowering ductility and fostering early strain localization [71]. Given that ductility is a controlling factor in the LCF regime, reduced ductility directly correlates with shorter fatigue life. Furthermore, irradiation-induced segregation and the accumulation of helium or point defects at grain boundaries can lead to embrittlement and intergranular cracking, exacerbating fatigue damage mechanisms [72] [55]. Other features appear to have less influence on the output, as indicated by the much narrower spread of the red/blue dots around the vertical partitioning line. However, this could be due to the less variability in their values in the utilized dataset. Additionally, Section S.5 of the Supplementary Materials showcase all models performance before and after removal of the highly correlated input features.

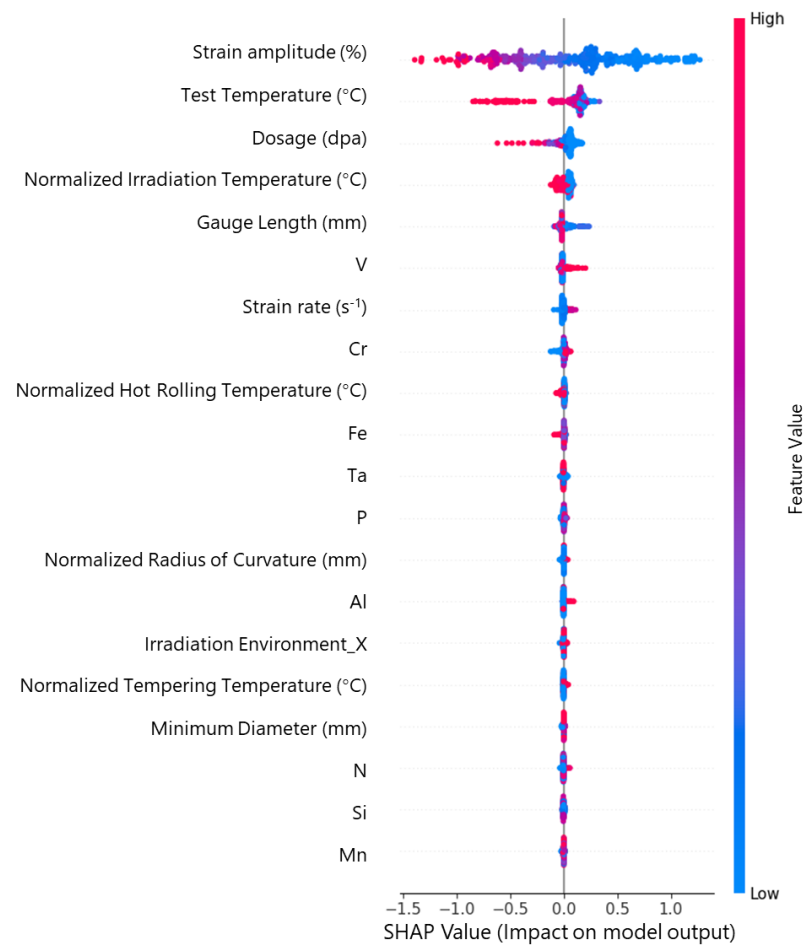


Fig. 4: SHAP summary plot showing the top 20 most influential input features affecting the predicted fatigue life in the PINN model. Each point represents the SHAP value of a single data instance, coloured by the corresponding feature value (red for high, blue for low). Points to the right of the vertical line indicate a positive contribution to the output, while those to the left indicate a negative impact. Greater horizontal spread and higher ranking strongly influence the model's predictions.

Overall, the SHAP analysis confirms that the PINN model captures physically meaningful complex dependencies, reinforcing its predictive accuracy with mechanistic fidelity. The alignment between model predictions and known deformation-fatigue mechanisms in irradiated materials underscores the utility of integrating domain knowledge into neural network frameworks for reliable fatigue life estimation.

3.3. Validation and trends obtained using synthetic data

Fig. 5 illustrates the predicted fatigue life (N) trends as a function of strain amplitude (S) for two alloys, SS316 (austenitic stainless steel), and F/M EUROFER97, using the developed PINN model. These predictions are based on univariate input trends, generated by systematically varying the irradiation dosage while keeping all other parameters constant. The test temperature was set at 300°C, representing typical service conditions in fission reactors. The irradiation dose ranges from the unirradiated condition up to 30 dpa, spanning the domain with sufficient experimental training data. The PINN model successfully captures key trends in fatigue degradation. As expected, fatigue life decreases with increasing strain amplitude across all alloys. In addition, increasing irradiation dose reduces fatigue life; however, the extent of degradation varies markedly among the alloys. SS316 shows a pronounced decline in cycles to failure with increasing doses, especially for a dosage of 30 dpa. In contrast, the F/M steel, EUROFER97, exhibits a modest decline in fatigue life with increasing irradiation dose, indicating greater tolerance to irradiation-induced degradation. In line with this outcome, fatigue-life data for irradiated reduced-activation F/M steels cluster around those of non-irradiated specimens, indicating minimal irradiation impact [58]. The enhanced irradiation tolerance observed in F/M steels can be attributed to their superior microstructural stability and resistance to void swelling. Mechanistically, this behavior is linked to enhanced point defect recombination at excess microstructural sinks such as solutes, precipitates/matrix interfaces, dislocation cores, grain boundaries, and the BCC crystal structure of the F/M steels. Additionally, a lower dislocation bias for self-interstitial absorption and reduced dislocation climb due to solute pinning [73–75]. These mechanisms collectively mitigate swelling and preserve fatigue performance under irradiation.

Overall, the PINN model demonstrates strong physical consistency in predicting fatigue degradation trends under reactor-relevant conditions. It highlights its potential utility for accelerated material screening and life assessment in nuclear environments.

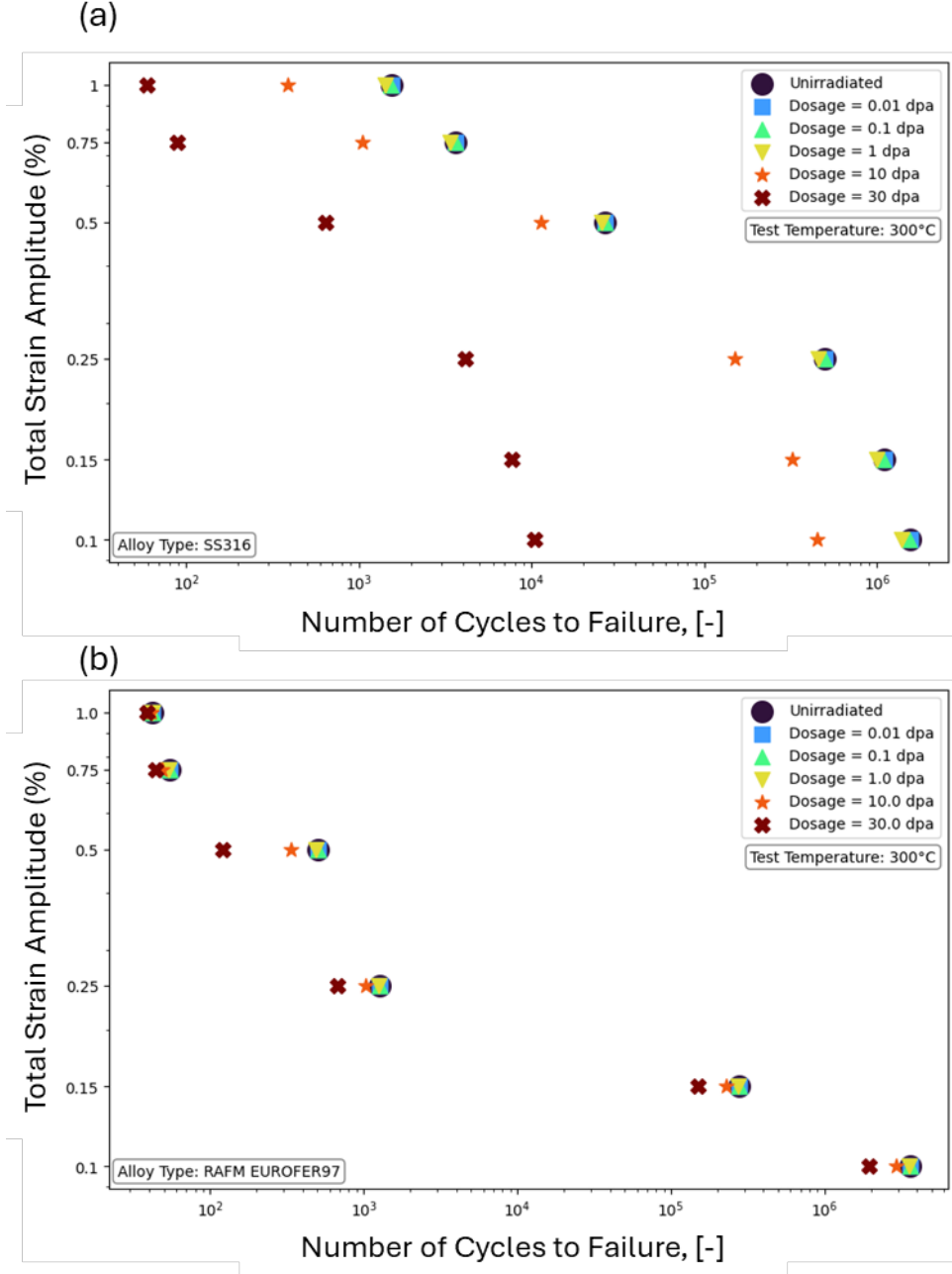


Fig. 5: Predicted S–N curves illustrating the effect of increasing irradiation dosage on fatigue life for (a) austenitic SS316, and (b) F/M EUROFER97 steels. A progressive reduction in the number of cycles to failure is observed with increasing dosage, with varying sensitivities across the two alloy systems.

4. Summary and conclusions

This study presents the first physics-informed neural network (PINN) framework for predicting LCF life in neutron-irradiated austenitic and ferritic/martensitic steels, thereby reducing reliance on extensive post-irradiation testing. Trained on a curated dataset of 495 strain-controlled fatigue data points, including both irradiated and unirradiated conditions, the model integrates 50 input features derived from the literature. The PINN framework

incorporates physical constraints via partial differential equations into the loss function, improving predictive fidelity while ensuring physical consistency. Compared to traditional ML models (such as RF, GB, XGB, NN), the PINN consistently demonstrated superior performance, achieving the highest average R^2 (0.85) and lowest average MSE (~ 0.07) across different data splits and random states. SHAP analysis validated the model's interpretability, revealing strain amplitude, irradiation dose, and test temperature as the most influential features, each showing a physically consistent inverse correlation with fatigue life. The model accurately captured known trends, such as the higher irradiation tolerance and dose saturation behavior in F/M steels compared to austenitic steels. These results align with experimental findings and the mechanistic understanding of irradiation effects, such as enhanced point defect recombination and reduced void swelling in F/M alloys.

Overall, the proposed PINN approach offers a robust, accurate, and interpretable tool for fatigue life prediction under irradiation. While promising, future work should focus on expanding the data to include broader material classes and irradiation conditions to validate further and generalize the model's applicability. Additionally, incorporating quantified microstructural features—such as dislocation density, irradiation-induced loop and void density, and grain size distribution—could further improve model fidelity by capturing irradiation-induced phenomena like defect clustering, helium bubble formation, and swelling on fatigue life.

Acknowledgements

AC gratefully acknowledges financial support from the IISc, Bengaluru and Infosys Foundation, Bangalore.

References

- [1] Allen T, Busby J, Meyer M, Petti D. Materials challenges for nuclear systems. *Materials Today* 2010;13:14–23. [https://doi.org/https://doi.org/10.1016/S1369-7021\(10\)70220-0](https://doi.org/10.1016/S1369-7021(10)70220-0).
- [2] Ullmaier H, Schilling W. Radiation damage in metallic reactor materials, Bundesministerium fuer Wissenschaft und Forschung.; 1980.
- [3] Was GS. Fundamentals of radiation materials science: Metals and alloys, second edition. Springer New York; 2016. <https://doi.org/10.1007/978-1-4939-3438-6>.

- [4] Klueh RL, Nelson AT. Ferritic/martensitic steels for next-generation reactors. *Journal of Nuclear Materials* 2007;371:37–52. <https://doi.org/10.1016/j.jnucmat.2007.05.005>.
- [5] Lehnen M, Aleynikova K, Aleynikov PB, Campbell DJ, Drewelow P, Eidietis NW, et al. Disruptions in ITER and strategies for their control and mitigation. *Journal of Nuclear Materials* 2015;463:39–48. <https://doi.org/10.1016/j.jnucmat.2014.10.075>.
- [6] Spolladore L, Rossi R, Wyss I, Gaudio P, Murari A, Gelfusa M. Detection of MARFES using visible cameras for disruption prevention. *Fusion Engineering and Design* 2023;190:113507. <https://doi.org/10.1016/j.fusengdes.2023.113507>.
- [7] Marmy P, Kruml T. Low cycle fatigue of Eurofer 97. *Journal of Nuclear Materials* 2008;377:52–8. <https://doi.org/10.1016/j.jnucmat.2008.02.054>.
- [8] Aktaa J, Petersen C. Modeling the constitutive behavior of RAFM steels under irradiation conditions. *Journal of Nuclear Materials* 2011;417:1123–6. <https://doi.org/10.1016/j.jnucmat.2010.12.295>.
- [9] Aktaa J, Schmitt R. High temperature deformation and damage behavior of RAFM steels under low cycle fatigue loading: Experiments and modeling. *Fusion Engineering and Design* 2006;81:2221–31. <https://doi.org/10.1016/j.fusengdes.2006.03.002>.
- [10] Aktaa J, Petersen C. Challenges in the constitutive modeling of the thermo-mechanical deformation and damage behavior of EUROFER 97. *Eng Fract Mech* 2009;76:1474–84. <https://doi.org/10.1016/j.engfracmech.2008.12.017>.
- [11] Führer U, Aktaa J. Modeling the cyclic softening and lifetime of ferritic-martensitic steels under creep-fatigue loading. *Int J Mech Sci* 2017. <https://doi.org/10.1016/j.ijmecsci.2017.12.042>.
- [12] Basquin OH. The exponential law of endurance tests. *Proceedings - American Society for Testing Materials* 1910;10:625–30.
- [13] Manson SS. Behavior of materials under conditions of thermal stress. Cleveland, OH, United States: 1954.
- [14] Coffin LF. A study of the effects of cyclic thermal stresses on a ductile metal. *Transaction of ASME* 1954;76:931–50.
- [15] Nogami S, Guan W, Toyota M, Hasegawa A. Fatigue life prediction of ferritic/martensitic steels based on universal slope equations and tensile properties obtained using small specimen. *Fusion Engineering and Design* 2017;125:330–6. <https://doi.org/10.1016/j.fusengdes.2017.04.036>.
- [16] Hirose T, Sakasegawa H, Nakajima M, Kato T, Miyazawa T, Tanigawa H. Effects of test environment on high temperature fatigue properties of reduced activation ferritic/martensitic steel, F82H. *Fusion Engineering and Design* 2018;136:1073–6. <https://doi.org/10.1016/j.fusengdes.2018.04.072>.
- [17] Hirose T, Kato T, Sakasegawa H, Tanigawa H, Nozawa T. Evaluation of fatigue properties of reduced activation ferritic/martensitic steel, F82H for development of

- design criteria. *Fusion Engineering and Design* 2020;160:111823.
<https://doi.org/10.1016/j.fusengdes.2020.111823>.
- [18] Wang C, Shen C, Cui Q, Zhang C, Xu W. Tensile property prediction by feature engineering guided machine learning in reduced activation ferritic/martensitic steels. *Journal of Nuclear Materials* 2020;529:151823.
<https://doi.org/10.1016/j.jnucmat.2019.151823>.
 - [19] Wang C, Shen C, Huo X, Zhang C, Xu W. Design of comprehensive mechanical properties by machine learning and high-throughput optimization algorithm in RAFM steels. *Nuclear Engineering and Technology* 2020;52:1008–12.
<https://doi.org/10.1016/j.net.2019.10.014>.
 - [20] Li X, Zheng M, Yang X, Chen P, Ding W. A property-oriented design strategy of high-strength ductile RAFM steels based on machine learning. *Materials Science and Engineering: A* 2022;840:142891. <https://doi.org/10.1016/j.msea.2022.142891>.
 - [21] Sai NJ, Rathore P, Chauhan A. Machine learning-based predictions of fatigue life for multi-principal element alloys. *Scr Mater* 2023;226:115214.
<https://doi.org/10.1016/j.scriptamat.2022.115214>.
 - [22] Bao H, Wu S, Wu Z, Kang G, Peng X, Withers PJ. A machine-learning fatigue life prediction approach of additively manufactured metals. *Eng Fract Mech* 2021;242:107508. <https://doi.org/10.1016/j.engfracmech.2020.107508>.
 - [23] Srinivasan V, Valsan M, Bhanu Shankar Rao K, Mannan SL, Raj B. Low cycle fatigue and creep–fatigue interaction behavior of 316L(N) stainless steel and life prediction by artificial neural network approach. *Int J Fatigue* 2003;25:1327–38.
[https://doi.org/10.1016/S0142-1123\(03\)00064-1](https://doi.org/10.1016/S0142-1123(03)00064-1).
 - [24] Agrawal A, Deshpande PD, Cecen A, Basavarsu GP, Choudhary AN, Kalidindi SR. Exploration of data science techniques to predict fatigue strength of steel from composition and processing parameters. *Integr Mater Manuf Innov* 2014;3:90–108.
<https://doi.org/10.1186/2193-9772-3-8>.
 - [25] Zhang M, Sun C-N, Zhang X, Goh PC, Wei J, Hardacre D, et al. High cycle fatigue life prediction of laser additive manufactured stainless steel: A machine learning approach. *Int J Fatigue* 2019;128:105194.
<https://doi.org/10.1016/j.ijfatigue.2019.105194>.
 - [26] Zhan Z, Li H. A novel approach based on the elastoplastic fatigue damage and machine learning models for life prediction of aerospace alloy parts fabricated by additive manufacturing. *Int J Fatigue* 2021;145:106089.
<https://doi.org/10.1016/j.ijfatigue.2020.106089>.
 - [27] He L, Wang Z, Akebono H, Sugeta A. Machine learning-based predictions of fatigue life and fatigue limit for steels. *J Mater Sci Technol* 2021;90:9–19.
<https://doi.org/10.1016/j.jmst.2021.02.021>.
 - [28] Liu Y, Wu H, Mayeshiba T, Afflerbach B, Jacobs R, Perry J, et al. Machine learning predictions of irradiation embrittlement in reactor pressure vessel steels. *NPJ Comput Mater* 2022;8:85. <https://doi.org/10.1038/s41524-022-00760-4>.

- [29] Kemp R, Cottrell GA, Bhadeshia HKDH, Odette GR, Yamamoto T, Kishimoto H. Neural-network analysis of irradiation hardening in low-activation steels. *Journal of Nuclear Materials* 2006;348:311–28.
<https://doi.org/10.1016/J.JNUCMAT.2005.09.022>.
- [30] Sai NJ, Rathore P, Sridharan K, Chauhan A. Machine learning-based predictions of yield strength for neutron-irradiated ferritic/martensitic steels. *Fusion Engineering and Design* 2023;195:113964. <https://doi.org/10.1016/j.fusengdes.2023.113964>.
- [31] Lee GG, Kim MC, Lee BS. Machine learning modeling of irradiation embrittlement in low alloy steel of nuclear power plants. *Nuclear Engineering and Technology* 2021;53:4022–32. <https://doi.org/10.1016/J.NET.2021.06.014>.
- [32] Xu C, Liu X, Wang H, Li Y, Jia W, Qian W, et al. A study of predicting irradiation-induced transition temperature shift for RPV steels with XGBoost modeling. *Nuclear Engineering and Technology* 2021;53:2610–5.
<https://doi.org/10.1016/J.NET.2021.02.015>.
- [33] Jin M, Cao P, Short MP. Predicting the onset of void swelling in irradiated metals with machine learning. *Journal of Nuclear Materials* 2019;523:189–97.
<https://doi.org/10.1016/J.JNUCMAT.2019.05.054>.
- [34] Sai NJ, Sridharan K, Chauhan A. Establishing machine-learning approach for predicting outer-diametral strains in ferritic/martensitic (F/M) steel tubes during in-reactor neutron-irradiation creep experiments. *Progress in Nuclear Energy* 2024;177:105418. <https://doi.org/10.1016/j.pnucene.2024.105418>.
- [35] Zahran H, Zinovev A, Terentyev D, Aouf A, Abdel Wahab M. Low cycle fatigue life prediction for neutron-irradiated and nonirradiated RAFM steels via machine learning. *Fusion Engineering and Design* 2025;221:115394.
<https://doi.org/10.1016/j.fusengdes.2025.115394>.
- [36] Zahran H, Zinovev A, Terentyev D, Aiello G, Abdel Wahab M. Prediction of low cycle fatigue life for neutron-irradiated and nonirradiated RAFM steels using their tensile properties. *Int J Fatigue* 2025;190:108589.
<https://doi.org/10.1016/j.ijfatigue.2024.108589>.
- [37] Tanigawa H. Technical challenges on material and design criteria development for fusion in-vessel components. *Fusion Engineering and Design* 2018;133:89–94.
<https://doi.org/10.1016/j.fusengdes.2018.05.047>.
- [38] Hao WQ, Tan L, Yang XG, Shi DQ, Wang ML, Miao GL, et al. A physics-informed machine learning approach for notch fatigue evaluation of alloys used in aerospace. *Int J Fatigue* 2023;170. <https://doi.org/10.1016/j.ijfatigue.2023.107536>.
- [39] Lian Z, Li M, Lu W. Fatigue life prediction of aluminum alloy via knowledge-based machine learning. *Int J Fatigue* 2022;157.
<https://doi.org/10.1016/j.ijfatigue.2021.106716>.
- [40] Zhang XC, Gong JG, Xuan FZ. A physics-informed neural network for creep-fatigue life prediction of components at elevated temperatures. *Eng Fract Mech* 2021;258.
<https://doi.org/10.1016/j.engfracmech.2021.108130>.

- [41] Chen J, Liu Y. Probabilistic physics-guided machine learning for fatigue data analysis. *Expert Syst Appl* 2021;168. <https://doi.org/10.1016/j.eswa.2020.114316>.
- [42] Zhou T, Jiang S, Han T, Zhu SP, Cai Y. A physically consistent framework for fatigue life prediction using probabilistic physics-informed neural network. *Int J Fatigue* 2023;166. <https://doi.org/10.1016/j.ijfatigue.2022.107234>.
- [43] Yang J, Kang G, Kan Q. Rate-dependent multiaxial life prediction for polyamide-6 considering ratchetting: Semi-empirical and physics-informed machine learning models. *Int J Fatigue* 2022;163. <https://doi.org/10.1016/j.ijfatigue.2022.107086>.
- [44] Fan J Le, Zhu G, Zhu ML, Xuan FZ. A data-physics integrated approach to life prediction in very high cycle fatigue regime. *Int J Fatigue* 2023;176. <https://doi.org/10.1016/j.ijfatigue.2023.107917>.
- [45] Salvati E, Tognan A, Laurenti L, Pelegatti M, De Bona F. A defect-based physics-informed machine learning framework for fatigue finite life prediction in additive manufacturing. *Mater Des* 2022;222. <https://doi.org/10.1016/j.matdes.2022.111089>.
- [46] He GY, Zhao YX, Yan CL. Multiaxial fatigue life prediction using physics-informed neural networks with sensitive features. *Eng Fract Mech* 2023;289. <https://doi.org/10.1016/j.engfracmech.2023.109456>.
- [47] Debgodan CE. Tensile and fatigue data for irradiated and unirradiated AISI 310 stainless steel and titanium-5 percent aluminum-2.5 percent tin: Application of the method of universal slopes. 1973.
- [48] Materna-Morris E, Möslang A, Schneider HC. Tensile and low cycle fatigue properties of EUROFER97-steel after 16.3 dpa neutron irradiation at 523, 623 and 723 K. *Journal of Nuclear Materials* 2013;442. <https://doi.org/10.1016/j.jnucmat.2013.03.038>.
- [49] Grossbeck ML, Vitek JM, Liu KC. Fatigue behavior of irradiated helium-containing ferritic steels for fusion reactor applications. *Journal of Nuclear Materials* 1986;141–143:966–72. [https://doi.org/10.1016/0022-3115\(86\)90126-1](https://doi.org/10.1016/0022-3115(86)90126-1).
- [50] Nogami S, Hasegawa A, Yamazaki M. Fatigue properties of ferritic/martensitic steel after neutron irradiation and helium implantation. *Nuclear Materials and Energy* 2020;24. <https://doi.org/10.1016/j.nme.2020.100764>.
- [51] Miwa Y, Jitsukawa S, Yonekawa M. Fatigue properties of F82H irradiated at 523 K to 3.8 dpa. *Journal of Nuclear Materials*, vol. 329–333, 2004, p. 1098–102. <https://doi.org/10.1016/j.jnucmat.2004.04.029>.
- [52] Ioka I, Yonekawa M, Miwa Y, Mimura H, Tsuji H, Hoshiya T. Effect of helium to dpa ratio on fatigue behavior of austenitic stainless steel irradiated to 2 dpa. n.d. [https://doi.org/https://doi.org/10.1016/S0022-3115\(00\)00209-9](https://doi.org/https://doi.org/10.1016/S0022-3115(00)00209-9).
- [53] Vandermeulen W, Hendrix W, Massaut V, Van De Velde J. The effect of neutron irradiation on the fatigue behaviour of AISI 316L-Results of first in-pile tests. vol. 183. 1991.

- [54] Brinkman C, Korth G, Beeston J. Influence of Irradiation on the Creep/Fatigue Behavior of Several Austenitic Stainless Steels and Incoloy 800 at 700 C. Effects of Radiation on Substructure and Mechanical Properties of Metals and Alloys, ASTM International 100 Barr Harbor Drive, PO Box C700, West Conshohocken, PA 19428-2959; 1973, p. 473–90. <https://doi.org/10.1520/STP35469S>.
- [55] Beeston J, Brinkman C. Axial Fatigue of Irradiated Stainless Steels Tested at Elevated Temperatures. Irradiation Effects on Structural Alloys for Nuclear Reactor Applications, ASTM International 100 Barr Harbor Drive, PO Box C700, West Conshohocken, PA 19428-2959; 1970, p. 419–48. <https://doi.org/10.1520/STP26641S>.
- [56] Gaganidze E, Petersen C, Aktaa J, Povstyanko A, Prokhorov V, Diegele E, et al. Low cycle fatigue properties of reduced activation ferritic/martensitic steels after high-dose neutron irradiation. Nuclear Fusion 2011;51. <https://doi.org/10.1088/0029-5515/51/8/083012>.
- [57] Petersen C, Povstyanko A, Prokhorov V, Fedoseev A, Makarov O, Walter M. Tensile and low cycle fatigue properties of different ferritic/martensitic steels after the fast reactor irradiation “ARBOR 1.” Journal of Nuclear Materials 2009;386–388:299–302. <https://doi.org/10.1016/j.jnucmat.2008.12.112>.
- [58] Gaganidze E, Petersen C. Post irradiation examination of RAF/M steels after fast reactor irradiation up to 71 dpa and < 340°C (ARBOR 2) : RAFM steels: metallurgical and mechanical characterisation. (KIT Scientific Reports ; 7596). KIT Scientific Publishing; 2011. <https://doi.org/10.5445/KSP/1000023594>.
- [59] D McGinnis W, Siu C, S A, Huang H. Category Encoders: a scikit-learn-contrib package of transformers for encoding categorical data. The Journal of Open Source Software 2018;3:501. <https://doi.org/10.21105/joss.00501>.
- [60] Materials Reliability Program: Development of a Material Constitutive Model for Irradiated Austenitic Stainless Steels (MRP-135, Revision 2). EPRI, Palo Alto, 3002013216. 2019.
- [61] Raissi M, Perdikaris P, Karniadakis GE. Physics-informed neural networks: A deep learning framework for solving forward and inverse problems involving nonlinear partial differential equations. J Comput Phys 2019;378:686–707. <https://doi.org/10.1016/J.JCP.2018.10.045>.
- [62] Jiang L, Hu Y, Liu Y, Zhang X, Kang G, Kan Q. Physics-informed machine learning for low-cycle fatigue life prediction of 316 stainless steels. Int J Fatigue 2024;182. <https://doi.org/10.1016/j.ijfatigue.2024.108187>.
- [63] Huber PJ. Robust Estimation of a Location Parameter. The Annals of Mathematical Statistics 1964;35:73–101. <https://doi.org/10.1214/aoms/1177703732>.
- [64] Nakamura K, Derbel B, Won KJ, Hong BW. Learning-rate annealing methods for deep neural networks. Electronics (Switzerland) 2021;10. <https://doi.org/10.3390/electronics10162029>.

- [65] Stubbins JF, Gelles DS. Fatigue performance and cyclic softening of F82H, a ferritic-martensitic steel. *Journal of Nuclear Materials* 1996;233–237:331–5. [https://doi.org/10.1016/S0022-3115\(96\)00226-7](https://doi.org/10.1016/S0022-3115(96)00226-7).
- [66] Polák J, Mazánová V, Heczko M, Kuběna I, Man J. Profiles of persistent slip markings and internal structure of underlying persistent slip bands. *Fatigue Fract Eng Mater Struct* 2017;40:1101–16. <https://doi.org/10.1111/ffe.12567>.
- [67] Mughrabi H. Cyclic Slip Irreversibilities and the Evolution of Fatigue Damage. *Metallurgical and Materials Transactions A* 2009;40:1257–79. <https://doi.org/10.1007/s11661-009-9839-8>.
- [68] Armas AF, Petersen C, Schmitt R, Avalos M, Alvarez-Armas I. Mechanical and microstructural behaviour of isothermally and thermally fatigued ferritic/martensitic steels. *Journal of Nuclear Materials* 2002;307–311:509–13. [https://doi.org/10.1016/S0022-3115\(02\)01086-3](https://doi.org/10.1016/S0022-3115(02)01086-3).
- [69] Chauhan A, Hoffmann J, Litvinov D, Aktaa J. High-temperature low-cycle fatigue behavior of a 9Cr-ODS steel: Part 1 - pure fatigue, microstructure evolution and damage characteristics. *Materials Science and Engineering: A* 2017;707:207–20. <https://doi.org/10.1016/j.msea.2017.09.031>.
- [70] Fournier B, Maxime S, Christel C, Michel N, Véronique R, Annick B, et al. High temperature creep–fatigue–oxidation interactions in 9–12%Cr martensitic steels. *Journal of Nuclear Materials* 2009;386–388:418–21. <https://doi.org/10.1016/j.jnucmat.2008.12.139>.
- [71] Was GS. *Fundamentals of Radiation Materials Science*. Berlin, Heidelberg: Springer Berlin Heidelberg; 2007. <https://doi.org/10.1007/978-3-540-49472-0>.
- [72] Grossbeck ML, Liu KC. FATIGUE BEHAVIOR OF TYPE 316 STAINLESS STEEL IRRADIATED IN A MIXED SPECTRUM FISSION REACTOR FORMING HELIUM. *Nucl Technol* 1982;58:538–47. <https://doi.org/10.13182/NT82-A32987>.
- [73] Klueh RL, Ehrlich K, Abe F. Ferritic/martensitic steels: promises and problems. *Journal of Nuclear Materials* 1992;191–194:116–24. [https://doi.org/10.1016/S0022-3115\(09\)80018-4](https://doi.org/10.1016/S0022-3115(09)80018-4).
- [74] Cabet C, Dalle F, Gaganidze E, Henry J, Tanigawa H. Ferritic-martensitic steels for fission and fusion applications. *Journal of Nuclear Materials* 2019;523:510–37. <https://doi.org/10.1016/j.jnucmat.2019.05.058>.
- [75] Little EA. Void-swelling in irons and ferritic steels. *Journal of Nuclear Materials* 1979;87:11–24. [https://doi.org/10.1016/0022-3115\(79\)90122-3](https://doi.org/10.1016/0022-3115(79)90122-3).

Supplementary Materials

Physics-informed neural network for fatigue life prediction of irradiated austenitic and ferritic/martensitic steels

Dhiraj S. Kori¹, Abhinav Chandraker¹, Syed Abdur Rahman², Punit Rathore³ and Ankur Chauhan¹

¹Extreme Environments Materials Group, Department of Materials Engineering, Indian Institute of Science (IISc), Bengaluru, 560012 Karnataka, India

²Department of Materials, University of Oxford, Parks Road, Oxford, OX1 3PH, United Kingdom

³Robert Bosch Centre for Cyberphysical Systems, Indian Institute of Science (IISc), Bengaluru, 560012 Karnataka, India

*Corresponding author: ankurchauhan@iisc.ac.in

S.1: Composition of all the steels considered in this work from literature.

Table S.1: Composition of all the steels considered in this work from the literature [1–12].

Alloy	Element (Range)
SS304	C (0–0.08), Mn (0–2), P (0–0.045), S (0–0.03), Si (0–1), Cr (18–20), Ni (8–10.5), N (0–0.1)
SS304L	C (0–0.03), Mn (0–2), P (0–0.045), S (0–0.03), Si (0–1), Cr (18–20), Ni (8–12), N (0–0.1)
SS316	C (0.03–0.08), Mn (0–2), P (0–0.045), S (0–0.03), Si (0–1), Cr (16–18), Ni (10–14), Mo (2–3), N (0–0.1)
SS316L	C (0–0.03), Mn (0–2), P (0–0.045), S (0–0.03), Si (0–1), Cr (16–18), Ni (10–14), Mo (2–3), N (0–0.1)
SS310	C (0–0.25), Mn (0–2), P (0–0.045), S (0–0.03), Si (0–1.5), Cr (24–26), Ni (19–22)
F82H	C (0.08–0.12), Mn (0.05–0.21), P (0–0.01), S (0–0.01), Si (0.05–0.2), Cr (7.4–8.5), Ni (0–0.1), V (0.15–0.25), N (0–0.02), W (1.8–2.2), Ta (0.01–0.06), Mo (0–0.05), Ti (0–0.012)
EUROFER97	C (0.09–0.12), Mn (0.22–0.61), P (0–0.01), S (0–0.005), Si (0–0.1), Cr (8.5–9.5), Ni (0–0.05), V (0.15–0.25), W (1–1.3), Ta (0.055–0.95), Mo (0–0.05), Ti (0–0.01)
T91	C (0.07–0.14), Mn (0.3–0.6), P (0–0.02), S (0–0.01), Cr (8–9.5), Ni (0–0.4), Mo (0.8–1.05), V (0.18–0.25), Si (0–0.25), Al (0–0.013), Ti (0–0.01), Nb (0.06–0.1)

HT-9	C (0.17–0.23), Mn (0.4–0.7), Si (0.1–0.3), Cr (11–12.5), Mo (0.8–1.2), V (0.25–0.35), W (0.4–0.6)
OPTIFER IVc	C (0.1–0.13), Mn (0.42–0.6), P (0–0.01), S (0–0.005), Si (0–0.155), Cr (9.25–10.75), Ni (0–0.009), V (0.18–0.3), W (1–1.2), Ta (0.05–0.95), Mo (0–0.005), Ti (0–0.01)

Table S.2: Range of values for the input features [1–12].

Feature	Min Value	Max Value
Normalizing Temperature (°C)	950	1050
Normalizing Time (min)	10	60
Tempering Temperature (°C)	700	780
Tempering Time (min)	30	300
Hot Rolling Temperature (°C)	1050	1200
Annealing Temperature (°C)	929	1070
Annealing Time (min)	15	60
Additional Pre-treatments	Solution-annealed	
	HS-CS	
	Cold worked (CW)- 13 %	
	CST	
	Cold worked (CW) - 11 %	
	Austenitized	
Dosage (dpa)	0	71
Test temperature (°C)	22	700
Strain amplitude (%)	0.14	6.15
Cycles to failure	11	247907
Sample Type	Hourglass	
	Cylinder	
Minimum Diameter (mm)	1.25	5.1
Gauge Length (mm)	6	25.6
Radius of Curvature (mm)	10	inf
Strain rate (s ⁻¹)	0.003	0.8
Irradiation Temperature (°C)	55	750

S.2: Brief descriptions of the employed ML algorithms

S.2.1: Artificial Neural Networks

Artificial Neural Networks (ANN) are a class of ML algorithms inspired by the structure and function of the human brain [13]. They consist of interconnected layers of artificial neurons that process input data and produce output predictions. ANNs comprise input, hidden, and output layers (see Fig. S.1). The input layer receives the initial feature vector and transmits it to the hidden layers, where a weighted sum of the input data is performed. The output layer generates predictions or classifications. Training involves iterative processes that adjust the weights and biases, enabling accurate predictions on unseen data.

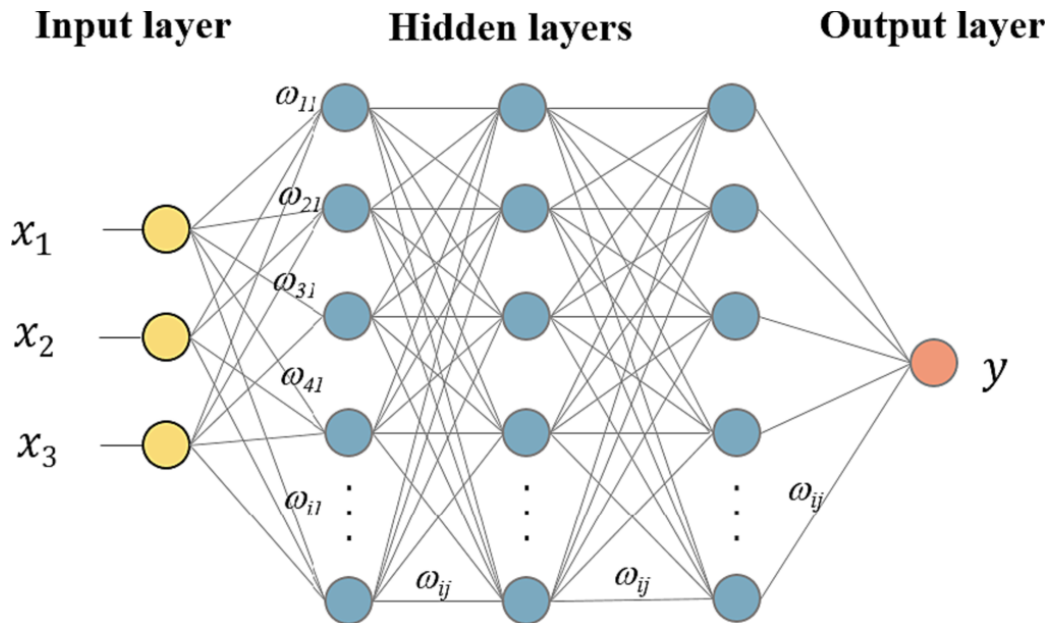


Fig. S.1: Architecture of a Neural Network showcasing Input, Hidden, and Output Layers.

A feedforward NN architecture was defined using the library PyTorch [14]. Some of its key components are described:

- **Input Layer:** The network takes the input of dimension `input_dim` (the number of neurons)
- **Hidden Layers:** It consists of two hidden layers, each with dimensions `hidden_dim1` and `hidden_dim2` (the number of neurons). Increasing the values of the dimensions allows the network to learn more complex patterns in the data and increases the risk of overfitting if not correctly regularised.

- **Activation Function:** The activation function used between the layers introduces non-linearity and thus preserves the mean and variance of data during training, potentially reducing the need for batch normalization. Some of the activation functions used are Hyperbolic Tangent (Tanh), Sigmoid Linear Unit (SiLU), Exponential Linear Unit (ELU), Rectified Linear Unit (ReLU), and Gaussian Error Linear Unit (GELU). The activation function used in this model is the Scaled Exponential Linear Unit (SELU) (see Fig. S2), which helps in faster convergence [15].

$$\text{SELU}(x) = \lambda \begin{cases} x & , x > 0 \\ \alpha(e^x - 1) & , x \leq 0 \end{cases}$$

Where:

$$\lambda \approx 1.05074$$

$$\alpha \approx 1.67326$$

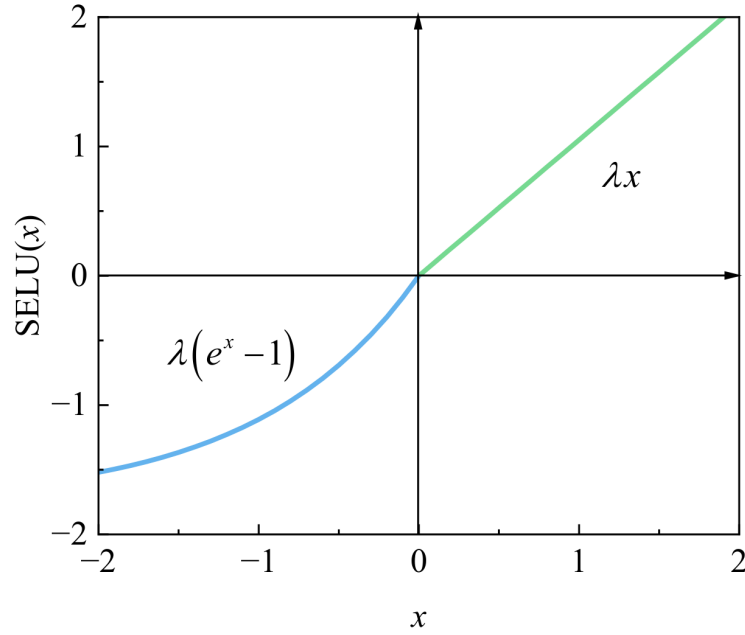


Fig. S.2: Graph of the activation function, SELU(x) vs x [16]. X is the output of the hidden layer for the activation function, SELU (x).

- **Output Layer:** The output layer has a single neuron representing the predicted value. The calculation process in each neuron can be represented as:

$$a = f\left(\sum (w \times x) + b\right)$$

Where:

a: Output

w: Weight

x: Input

b: Bias

f: Activation Function

For the entire NN, the process of summing the weighted inputs of neurons can be represented as:

$$z_j^{(n)} = \sum_i (w_{j \times i}^{(n)} \cdot x_i) + b_j^{(n)}$$
$$Z_{j \times 1}^{(n)} = \begin{cases} W_{j \times 1}^{(1)} \times X_{i \times 1} + B_{j \times 1}^{(1)}, & n = 1 \\ W_{j \times 1}^{(n)} \times A_{j \times 1}^{(n-1)} + B_{j \times 1}^{(n)}, & n > 1 \end{cases}$$

Where:

i: Number of neurons in the previous layer. If the hidden layer is considered first, it represents the number of input features.

j: Number of neurons in current layer

n: Level of the hidden layer

$$X_{i \times 1} = \begin{bmatrix} x_1 \\ x_2 \\ \vdots \\ x_i \end{bmatrix} : \text{Input layer matrix}$$

$$W_{j \times i}^{(n)} = \begin{bmatrix} w_{1 \times 1}^{(n)} & w_{1 \times 2}^{(n)} & \cdots & w_{1 \times i}^{(n)} \\ w_{2 \times 1}^{(n)} & w_{2 \times 2}^{(n)} & \cdots & w_{2 \times i}^{(n)} \\ \vdots & \vdots & \ddots & \vdots \\ w_{j \times 1}^{(n)} & w_{j \times 2}^{(n)} & \cdots & w_{j \times i}^{(n)} \end{bmatrix} : \text{Weight matrix of } n^{\text{th}} \text{ hidden layer}$$

$$B_{j \times 1}^{(n)} = \begin{bmatrix} b_1^{(n)} \\ b_2^{(n)} \\ \vdots \\ b_j^{(n)} \end{bmatrix} : \text{Bias matrix of } n^{\text{th}} \text{ hidden layer}$$

The output values of the n^{th} hidden layer after passing through an activation function are:

$$a_j^{(n-1)} = f_{n-1} \left(z_j^{(n-1)} \right)$$

$$A_{j \times 1}^{(n-1)} = f_{n-1} \left(Z_{j \times 1}^{(n-1)} \right)$$

Where $A_{j \times 1}^{(n)}$ is the weighted Output of n^{th} hidden layer and $Z_{j \times 1}^{(n)}$ is the weighted Sum of n^{th} hidden layer

Final Output of the NN, Y is given by:

$$y = f_m \left(\sum_i \left(w_{m \times i}^{(k)} \cdot a_i \right) + b_m^{(k)} \right)$$

$$Y = f_m \left(Z_{k \times 1}^{(m)} \right)$$

Where m is number of layers in the final hidden layer and k is the number of outputs

S.2.2: Random Forests:

Random Forest (RF) is a robust ensemble learning algorithm that builds multiple decision trees (DTs) to make predictions. It follows the *divide-and-conquer* strategy to enhance predictive performance and address the overfitting issues commonly associated with using a single decision tree [17]. DTs partition the feature space into regions based on simple decision rules, and each DT in a Random Forest comprises *decision nodes*, which apply decision-making rules, and *leaf nodes*, which contain the final outcomes [18]. RF uses a technique called *bootstrapping to ensure diversity among the DTs*, where each tree is trained on a different subset of the training data sampled *with replacement*. This process introduces randomness and reduces model variance.

For regression tasks, the final output is obtained through a voting mechanism or by averaging the predictions from all individual trees. This averaging mechanism helps reduce overfitting by smoothing out the predictions and mitigating the influence of any single overfit tree.

Key hyperparameters in Random Forest that influence its complexity and performance include:

- **Maximum depth** of the trees (controls how deep each tree can grow),
- **Maximum number of features** considered for splitting at each decision node (introduces randomness and prevents dominant features from being overused),

- **Number of trees** in the ensemble (controls the model's capacity and stability).

By tuning these hyperparameters appropriately, the RF algorithm can achieve high accuracy while maintaining generalization across unseen data.

S.2.3: Gradient Boosting:

Gradient Boosting (GB) is an ensemble-based algorithm that constructs models sequentially using DTs, and it differs fundamentally from the RF algorithm. While RF builds multiple deep and independent trees in parallel, GB constructs relatively shallow DTs, also known as 'Weak Learners', in sequence, creating a single 'Strong Learner', with each tree attempting to correct the errors of its predecessor [18].

The GB process begins by computing the average of the target values across the training data. This average serves as the initial prediction for all data points. The algorithm then calculates the differences between actual and predicted values, called as the loss function, and trains the first decision tree to fit them. The predicted output is then updated by adding the contribution of this tree (scaled by a *learning rate*) to the initial prediction.

This procedure is repeated iteratively: in each step, a new decision tree is trained to predict the residual errors from the cumulative prediction of the previous trees. In doing so, the model gradually reduces the loss function, ultimately leading to improved predictive performance.

Key hyperparameters that influence the behaviour and performance of GB include:

- **Maximum depth** of each tree (controls the complexity of individual learners),
- **Learning rate** (scales each tree's contribution to the final prediction),
- **Number of trees** (determines how many iterations the boosting process runs).

The final prediction for each data point is obtained by aggregating the initial average with the weighted sum of all subsequent tree outputs. Mathematically, the final model output can be expressed as:

$$Final\ Prediction = \bar{y} + \sum_{i=1}^N \eta \cdot h_i(x)$$

Where \bar{y} is the average of the actual outputs (initial prediction), η is the learning rate, $h_i(x)$ is the prediction from the i -th decision tree, and N is the total number of trees.

S.2.4: eXtreme Gradient Boosting:

eXtreme Gradient Boosting (XGB) is an advanced ensemble algorithm that builds upon the foundational principles of GB. While both algorithms operate by sequentially correcting errors from previous iterations, XGB introduces several enhancements in regularization, efficiency, and model structure.

Unlike traditional DTs, the trees in XGB employ a more sophisticated mechanism for node evaluation by incorporating the concept of the *Amount of Say*. This metric quantifies the influence or importance of each node in the decision-making process and plays a central role in determining the optimal splits.

The *Amount of Say* at each decision node is computed using the formula:

$$\text{Amount of Say} = \frac{(\sum g_i)^2}{\sum h_i + \lambda}$$

Where g_i is the first-order gradient (loss derivative), h_i is the second-order gradient (Hessian), and λ is the regularization parameter to control complexity.

The **gain** at a decision node, which measures the improvement in the loss function from a potential split, is given by:

$$\text{Gain} = \text{Amount of Say}_{\text{left child}} + \text{Amount of Say}_{\text{right child}} - \text{Amount of Say}_{\text{parent node}}$$

The algorithm selects splits that yield the highest gain, effectively focusing on nodes that lead to the greatest reduction in loss.

XGB introduces several important **hyperparameters** to control the model's learning and complexity:

- η : learning rate (controls step size in updates),
- λ : L^2 regularization term (prevents overfitting),
- γ : minimum loss reduction required to make a further partition on a leaf node (pruning parameter),
- `max_depth`: maximum depth of the trees,
- `n_estimators`: number of boosting rounds (trees in the ensemble).

Together, these improvements make XGB faster, more accurate, and more robust than standard GB.

S.2.5: SHapley Additive exPlanations

SHapley Additive exPlanations (SHAP) is a model-agnostic interpretability technique derived from cooperative game theory that quantifies the contribution of each input feature to a machine learning model's prediction [19]. It provides a principled way to understand the importance and influence of individual input features on the model's output, both globally (across the entire data) and locally (for each instance).

For any given prediction, SHAP assigns a SHAP value to every input feature. A larger SHAP value indicates a stronger influence of that feature on the output prediction, either positively or negatively. Importantly, SHAP does not just assess feature importance globally, but enables instance-level interpretability, making it possible to understand *how* each input feature contributed to a specific prediction.

To compute the SHAP value of a target feature for a given instance, the algorithm considers all possible subsets of input features that include the target feature. The model is evaluated on each of these subsets to estimate the prediction. Then, the target feature is removed, and the model is re-evaluated on the reduced subset. The difference in prediction reflects the marginal contribution of the target feature. SHAP aggregates these differences across all subsets using a weighted average based on the size of each subset.

Mathematically, the SHAP value for feature i with model f and instance x is defined as:

$$\Phi_i(f, x) = \sum_{S \subseteq [F - \{i\}]} \frac{|S|! (M - |S| - 1)!}{M!} [f_x(S \cup \{i\}) - f_x(S)]$$

Where $\Phi_{i(f,x)}$ is the SHAP value for feature i , S is a subset of the input feature set F , excluding feature i , M is the total number of input features, $f(S)$ is the model prediction using only the features in subset S , and $f(S \cup \{i\})$ is the prediction when feature i is added to subset S .

This equation ensures that each feature's contribution is distributed fairly based on its marginal impact across *all possible combinations*, aligning with the principles of Shapley values from cooperative game theory.

S.3: Hyperparameter Tuning - Bayesian Search Optimization

Hyperparameter tuning is the process of identifying the optimal combination of hyperparameters that yields the best performance for a given machine learning model on a specific dataset. Choosing the right hyperparameters is crucial, as they govern the model's capacity, learning dynamics, and overall generalization ability.

Traditional techniques like **Grid Search** and **Randomized Search** evaluate multiple hyperparameter combinations independently and without leveraging information from previous evaluations:

- Grid Search exhaustively explores all possible combinations within a predefined grid.
- Randomized Search samples a fixed number of random combinations from the hyperparameter space, offering faster results with potentially similar performance.

In contrast, **Bayesian Optimization** [17], introduces a more intelligent and efficient strategy by using prior evaluations to guide future exploration. It builds a **probabilistic surrogate model** (commonly a Gaussian Process Regression (GPR) or Tree-structured Parzen Estimator) to approximate the true objective function that maps hyperparameter sets to model performance.

This process iteratively evaluates the model's performance using different hyperparameter configurations, updates the surrogate model based on observed results, and selects the next set of hyperparameters to assess based on the acquisition function. This iterative process continues until a predefined stopping criterion is met, such as reaching a maximum number of iterations or achieving satisfactory performance.

Cross-validation is often employed to obtain reliable estimates of the model's performance for each hyperparameter configuration. Cross-validation involves:

- Partitioning the data into training and validation data,
- Training the model on the training data and
- Evaluating its performance on the validation data.

This process is repeated with different training-validation splits to mitigate overfitting and assess the model's robustness.

As a result, Bayesian search is typically faster and more robust than exhaustive or random search methods, especially when the evaluation of each model is computationally expensive.

Table S.3: Hyperparameter Search Space for the RF model.

RF	Hyperparameter Search Space
Min_samples_leaf	1 - 5
Min_samples_split	2 - 5
N_estimators	50-150

Table S.4: Hyperparameter Search Space for the GB model.

GBoost	Hyperparameter Search Space
lr	0.01-0.0001
Max depth	3-8
Min_samples_leaf	1-5
N_estimators	50-150

Table S.5: Hyperparameter Search Space for the XGBoost model.

XGBoost	Hyperparameter Search Space
Max depth	3-8
N_estimators	50-150
lr	0.0001-0.01
Gamma	0-0.0001
Lambda	1-3
Min_child_weight	3-8

Table S.6: Hyperparameter Search Space for the NN model.

NN	Hyperparameter Search Space
Hidden dim 1	100-120
Hidden dim 2	60-80
Hidden dim 3	20-40
Kappa	0.1-0.9
Batch size	20-50
Number of Epochs	900-1000

Weight Decay	0.001-0.1
--------------	-----------

Table S.7: Hyperparameter Search Space for the PINN model.

PINN	Hyperparameter Search Space
Hidden dim 1	100-120
Hidden dim 2	60-80
Hidden dim 3	20-40
Kappa	0.1-0.9
Batch size	20-50
Number of Epochs	900-1000
Weight Decay	0.001-0.1
Omega	0.01-0.99

S.4: Comparison of predicted vs. experimental fatigue life for training data

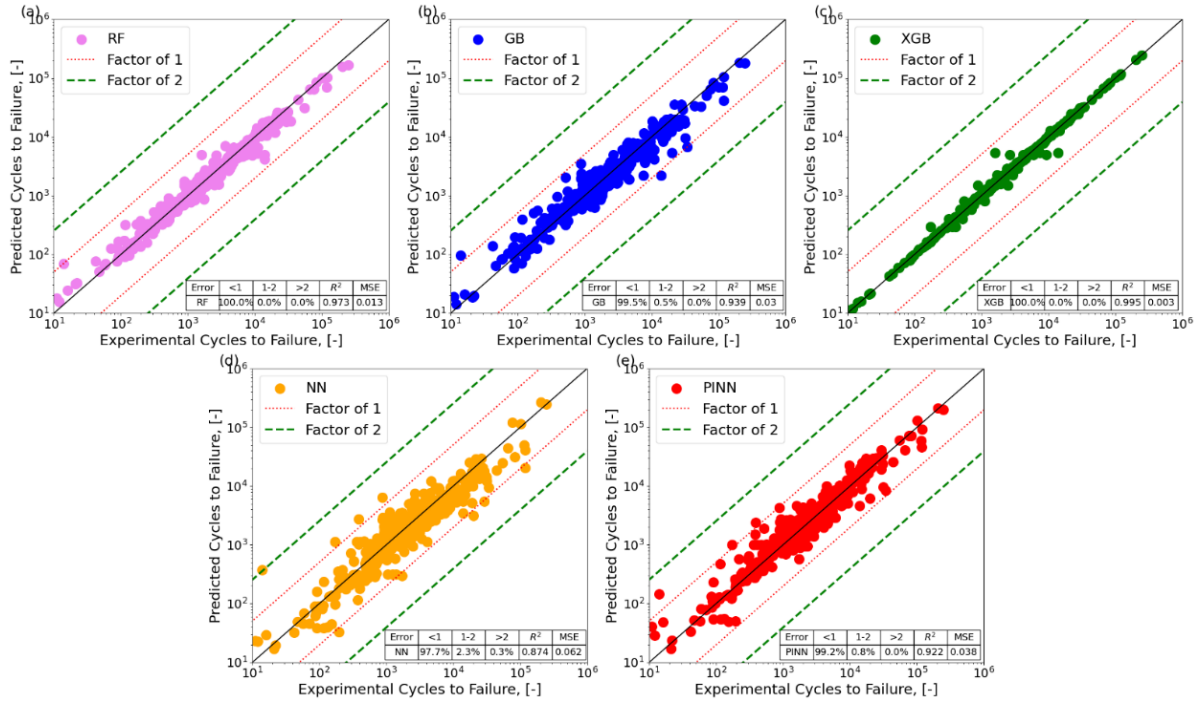


Fig S.4: Comparison of predicted vs. experimental fatigue life for the training data using (a) RF, (b) GB, (c) XGB, (d) NN, and (e) PINN models. Training data corresponds to the testing data for the 4th random state's 80:20 data split in the main file. The red dotted lines indicate the ± 1 error band, and the green dashed lines denote the ± 2 error band. The RF and XGB models are overfitting for the training data, while NN is underfitting.

Table S.8: Utilised Best Hyperparameters for different data splits for NN and PINN, obtained by Bayesian Search. The same hyperparameters are used for both NN and PINN models except Best Omega.

Random State	Data Split	Best Hidden Dim 1	Best Hidden Dim 2	Best Hidden Dim 3	Kappa	Batch Size	Number of Epochs	Weight Decay
1	80:20	100	60	34	0.9	44	900	0.004436
1	70:30	116	75	31	0.446	40	965	0.001795
2	80:20	118	71	34	0.891	30	932	0.00247
2	70:30	120	78	40	0.723	37	1000	0.002501
3	80:20	100	80	37	0.9	20	1000	0.001
3	70:30	100	61	20	0.9	20	900	0.002558
4	80:20	115	64	20	0.278	21	966	0.001164
4	70:30	100	65	30	0.1	30	1000	0.001

Table S.9: Accuracies (R^2) obtained for testing and training data for all the models used in benchmarking.

Random State	Data Split	Test NN R^2	Train NN R^2	Test RF R^2	Train RF R^2	Test GB R^2	Train GB R^2	Test XGB R^2	Train XGB R^2
1	80:20	0.784	0.915	0.841	0.976	0.799	0.949	0.833	0.997
1	70:30	0.789	0.914	0.840	0.974	0.827	0.949	0.849	0.998
2	80:20	0.765	0.905	0.797	0.975	0.790	0.946	0.771	0.996
2	70:30	0.753	0.858	0.806	0.972	0.820	0.946	0.832	0.996
3	80:20	0.872	0.921	0.895	0.975	0.886	0.935	0.901	0.996
3	70:30	0.836	0.900	0.872	0.975	0.877	0.940	0.867	0.996
4	80:20	0.849	0.874	0.866	0.973	0.851	0.939	0.847	0.995
4	70:30	0.815	0.921	0.826	0.968	0.815	0.941	0.838	0.995

Table S.10: Accuracies (MSE) obtained for testing and training data for all the models used in benchmarking.

Random State	Data Split	Test NN MSE	Train NN MSE	Test RF MSE	Train RF MSE	Test GB MSE	Train GB MSE	Test XGB MSE	Train XGB MSE
1	80:20	0.0958	0.0430	0.0706	0.0119	0.0892	0.0259	0.0742	0.0014
1	70:30	0.1085	0.0415	0.0824	0.0127	0.0888	0.0249	0.0775	0.0012
2	80:20	0.1145	0.0466	0.0990	0.0124	0.1025	0.0265	0.1115	0.0021
2	70:30	0.1248	0.0687	0.0978	0.0136	0.0910	0.0262	0.0848	0.0019
3	80:20	0.0439	0.0417	0.0362	0.0134	0.0392	0.0344	0.0340	0.0019
3	70:30	0.0580	0.0549	0.0451	0.0137	0.0436	0.0328	0.0470	0.0020
4	80:20	0.0739	0.0624	0.0656	0.0132	0.0726	0.0304	0.0748	0.0027
4	70:30	0.0958	0.0383	0.0901	0.0156	0.0957	0.0284	0.0839	0.0022

Table S.11: Accuracies (R^2 and MSE) obtained for testing and training data for PINN alongside the Best omega (obtained through Bayesian Search) used in its calculation.

Random State	Data Split	Best omega in (0.01-0.99)	Test PINN R^2	Train PINN R^2	Test PINN MSE	Train PINN MSE
1	80:20	0.05	0.820	0.922	0.0800	0.0393
1	70:30	0.23	0.847	0.905	0.0784	0.0462
2	80:20	0.09	0.820	0.913	0.0879	0.0428
2	70:30	0.19	0.832	0.920	0.0849	0.0386
3	80:20	0.11	0.863	0.908	0.0470	0.0490
3	70:30	0.21	0.860	0.901	0.0495	0.0545
4	80:20	0.02	0.880	0.889	0.0588	0.0548
4	70:30	0.1	0.851	0.931	0.0769	0.0335

S.5: Input-Feature Selection for Dimensionality Reduction

Feature selection was conducted in two steps. First, the most highly correlated features were removed to reduce redundancy, using a threshold value of 0.7. In this step, the feature with lower variance from each highly correlated pair was removed. The correlation matrix maps are shown in Fig. S.5. This process reduced the initial 50 features to 23, with 27 features being removed.

It was observed that all five models employed have slightly reduced average accuracy after feature removal. RF, GBoost and XGBoost consistently showed higher average accuracy than PINN, with NN being the worst performer, as shown in Fig. S.6. Meanwhile, PINN shows the least variance over all the other models similar to the PINN model performed on all the input features. This shows that the PINN model shows a higher sensitivity to the absence of input features, signifying that this model requires the mathematically obtained correlated features, as removing them leads to a loss of information, which other models are unable to capture. This might also be interpreted as PINN is not overfit to “highly ranked” input features obtained from SHAP and is utilizing most of the features to increase its predictive accuracy.

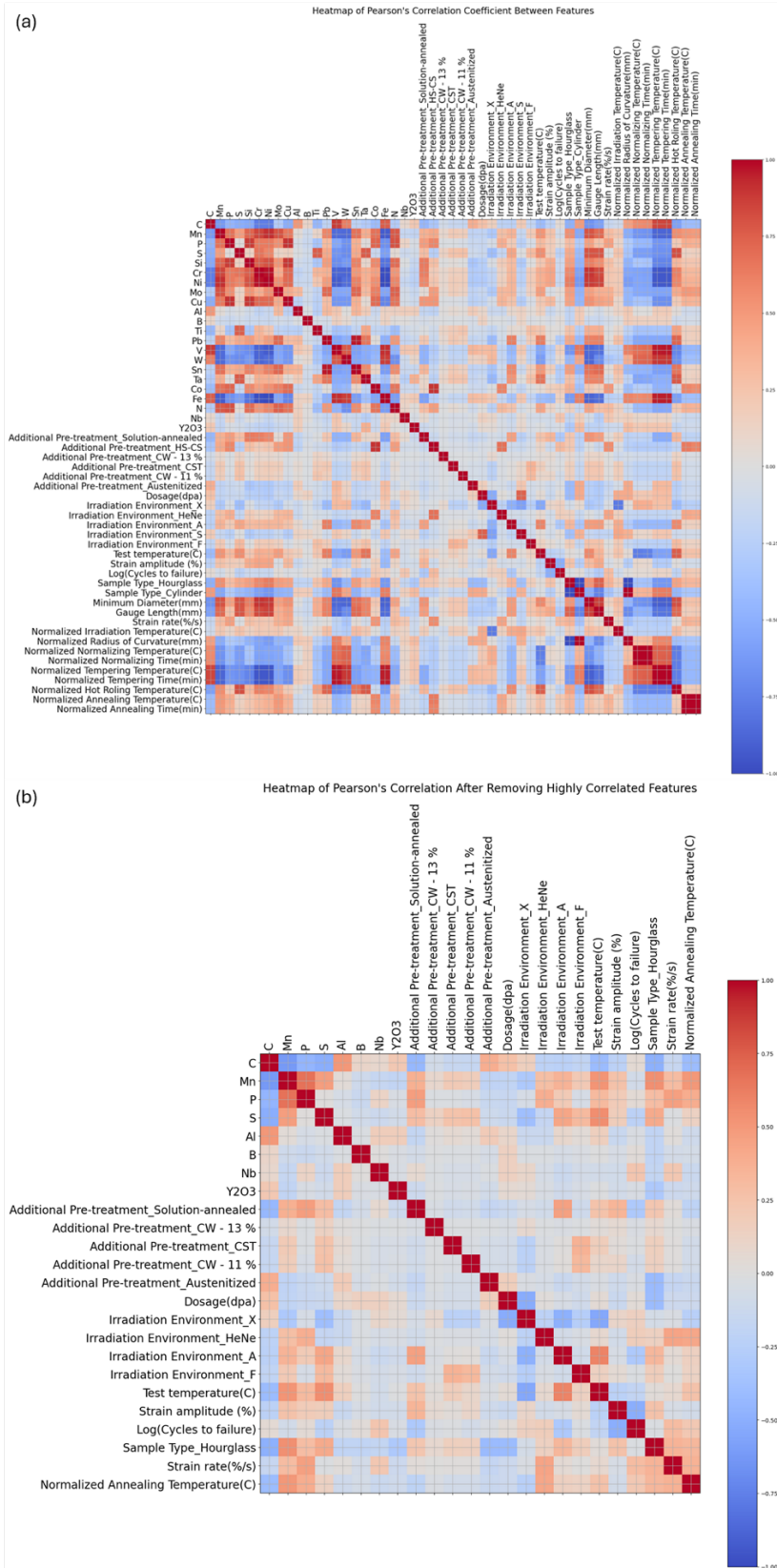


Fig. S.5: Visualization of Pearson's correlation coefficients considering (a) all the input features, (b) Input features obtained after the elimination of the features with lower variance from each highly correlated pair.

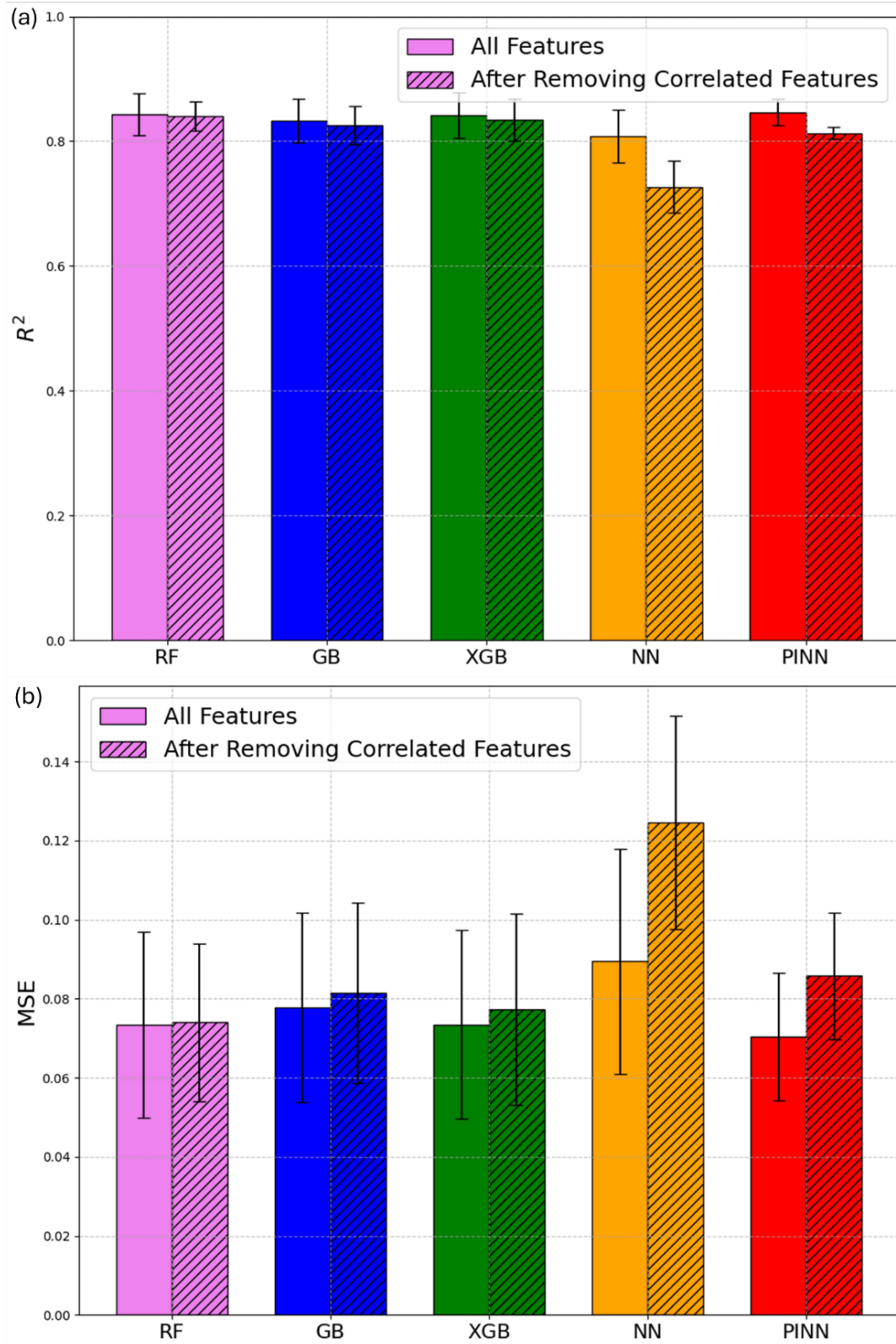


Fig. S.6: The average (a) R^2 and (b) MSE values for 5 predictive models before and after the removal of highly correlated input features: RF, GBoost, XGBoost, NN, and PINN tested across the combinations of all random states (1 to 4) and data-splits (70:30 and 80:20), shown with error bars representing the variance.

S.6: Visualizing the Impact of the Hyperparameter Beta on the PINN

The influence of the hyperparameter β (beta) on model performance (R^2 and MSE) was assessed using five randomly generated hyperparameter sets, each derived from the defined search space bounds. The beta values tested were 1, 10, 100, 1000, and 10000; among these, 1, 10, and 100 were previously employed in Jiang et al. [16], while 1000 and 10000 were included to confirm that arbitrarily increasing beta does not necessarily enhance accuracy. For every combination of hyperparameter set and beta value, models were trained over multiple random states and data splits. Importantly, no hyperparameter was specifically tuned for any given beta, this prevents the results from being biased toward any β , allowing the observed differences in R^2 and MSE to be attributed solely to changes in β rather than to simultaneous adjustments in other model settings. Lower R^2 (0.2-0.5) for test and train data is expected as none of the hyperparameters are tuned.

The results as illustrated in Fig. 7, where the mean R^2 and MSE across all datasets are shown, accompanied by error bars representing their standard deviations. It was observed that Beta = 100 yields the highest average accuracy along with the least variability amongst the other values. This behaviour can be explained by the structure of the PINN loss function, which is the sum of the neural network's data-fitting loss and the PDE-residual loss. From Equations (3) and (7) in the main script:

$$G(x) = \frac{x}{1 + e^{\beta|x|}} \quad (1)$$

$$\begin{aligned} \text{LOSS}_{\text{PDE}} = & \mathcal{L}\left(0, G_{\text{out}}\left(\frac{\partial N}{\partial \epsilon}\right)\right) + \mathcal{L}\left(0, G_{\text{out}}\left(\frac{\partial^2 N}{\partial \epsilon^2}\right)\right) + \mathcal{L}\left(0, G_{\text{out}}\left(\frac{\partial N}{\partial T}\right)\right) \\ & + \mathcal{L}\left(0, G_{\text{out}}\left(\frac{\partial N}{\partial d}\right)\right) \end{aligned} \quad (2)$$

As β increases, the output of $G(x)$ approaches zero, causing the PDE-residual loss to diminish. This weakens the physics constraints in the PINN, reducing its ability to generalize according to the governing equations and thereby lowering accuracy. Conversely, when β is too small, the PDE-residual loss becomes dominant, which can cause the model to overemphasize the physics constraints while neglecting noisy or imperfect training data, leading to higher error

and reduced accuracy. The value $\beta = 100$ appears to strike an optimal balance between data fidelity and physics consistency, resulting in superior and more stable performance.

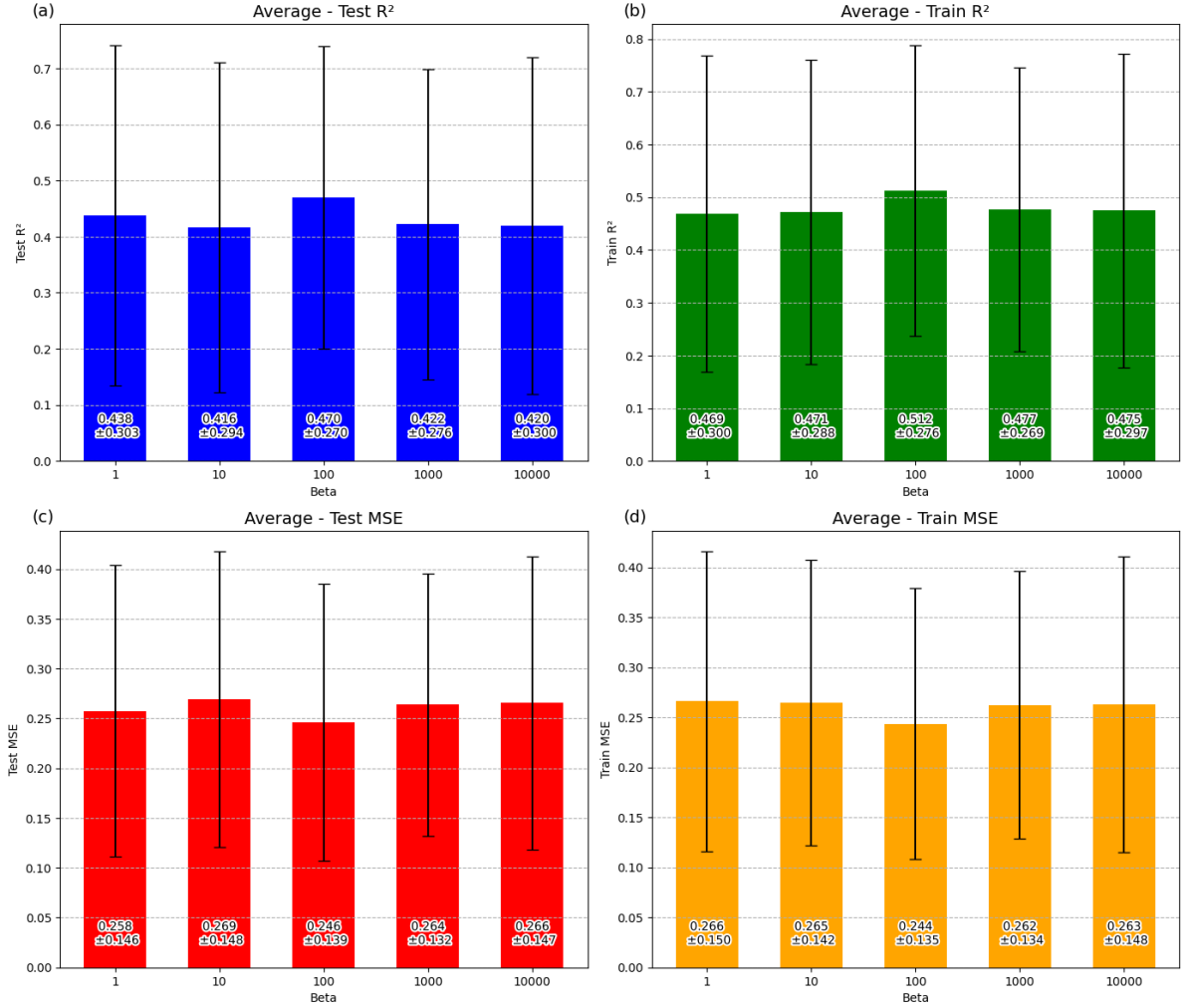


Fig. S.7: Bar plots showing the average values with standard deviation error bars for (a) Test R², (b) Train R², (c) Test MSE, and (d) Train MSE, obtained by varying the hyperparameter β across multiple random states, data splits, and randomized hyperparameter sets. The β values considered are 1, 10, 100, 1000, and 10000. Text within each bar indicates the average value along with its standard deviation. Notably, Beta = 100 yields the highest average performance with the lowest variability.

S.7: Derivation of First- and Second-Order Derivatives in the Neural Network

In the implementation of the Physics-Informed Neural Network (PINN), evaluation of the PDE residual requires computation of both the first and second-order derivatives of the network output y with respect to the input variables x_i . Since y is obtained through a composition of

multiple neural network layers, these derivatives are computed using repeated application of the chain rule across all layers.

Let $z^{(l)}$ denote the pre-activation vector at the l -th layer, and $a^{(l)}$ its activation output. For clarity, neuron indices at each layer are denoted as m, n, p, q . The forward pass of the network can be represented as:

$$x \rightarrow z^{(1)} \rightarrow a^{(1)} \rightarrow z^{(2)} \rightarrow a^{(2)} \dots \rightarrow z^{(l)} \rightarrow a^{(l)} \rightarrow \dots \rightarrow z^{(k)} \rightarrow y$$

Where

$$z_m^{(l)} = \sum_i \left(w_{m \times i}^{(l)} \cdot a_i^{(l-1)} \right) + b_m^{(l)}$$

$$a^{(l)} = f^{(l)}(z^{(l)}); a^{(0)} = x; a^{(k)} = y$$

Here, each summation accounts for the fact that all neurons in each layer contribute to the derivative via their weighted connections, which means that y is a nested composition. The first partial derivative of y with respect to an input x_i is obtained by propagating sensitivities

backward through the network. Starting from the output layer, we get: $\frac{\partial y}{\partial x_i} = \sum_m \frac{\partial y}{\partial z_m^{(k)}} \frac{\partial z_m^{(k)}}{\partial x_i}$

The output layer's pre-activation $z_m^{(k)}$ depends on the activations from the previous layers $a_n^{(k-1)}$:

$$\frac{\partial z_m^{(k)}}{\partial x_i} = \sum_n \frac{\partial z_m^{(k)}}{\partial a_n^{(k-1)}} \frac{\partial a_n^{(k-1)}}{\partial x_i}$$

But;

$$\frac{\partial a_n^{(k-1)}}{\partial x_i} = \frac{\partial a_n^{(k-1)}}{\partial z_n^{(k-1)}} \frac{\partial z_n^{(k-1)}}{\partial x_i}$$

Repeating this process until we reach the input layer, $l = 0$, we get the final expression:

$$\frac{\partial y}{\partial x_i} = \sum_m \frac{\partial y}{\partial z_m^{(k)}} \sum_n \frac{\partial z_m^{(k)}}{\partial a_n^{(k-1)}} \frac{\partial a_n^{(k-1)}}{\partial z_n^{(k-1)}} \dots \sum_p \frac{\partial z_r^{(3)}}{\partial a_p^{(2)}} \frac{\partial a_p^{(2)}}{\partial z_p^{(2)}} \sum_q \frac{\partial z_p^{(2)}}{\partial a_q^{(1)}} \frac{\partial a_q^{(1)}}{\partial z_q^{(1)}} \frac{\partial z_q^{(1)}}{\partial x_i}$$

Since our output layer has only one neuron:

$$\frac{\partial y}{\partial x_i} = \frac{\partial y}{\partial z_m^{(k)}} \sum_n \frac{\partial z_m^{(k)}}{\partial a_n^{(k-1)}} \frac{\partial a_n^{(k-1)}}{\partial z_n^{(k-1)}} \dots \sum_p \frac{\partial z_r^{(3)}}{\partial a_p^{(2)}} \frac{\partial a_p^{(2)}}{\partial z_p^{(2)}} \sum_q \frac{\partial z_p^{(2)}}{\partial a_q^{(1)}} \frac{\partial a_q^{(1)}}{\partial z_q^{(1)}} \frac{\partial z_q^{(1)}}{\partial x_i}$$

Further differentiating this expression:

$$\frac{\partial^2 y}{\partial x_i^2} = \left[\frac{\partial y}{\partial z_m^{(k)}} \right]' \sum_n \frac{\partial z_m^{(k)}}{\partial a_n^{(k-1)}} \frac{\partial a_n^{(k-1)}}{\partial z_n^{(k-1)}} \cdots \sum_p \frac{\partial z_r^{(3)}}{\partial a_p^{(2)}} \frac{\partial a_p^{(2)}}{\partial z_p^{(2)}} \sum_q \frac{\partial z_p^{(2)}}{\partial a_q^{(1)}} \frac{\partial a_q^{(1)}}{\partial z_q^{(1)}} \frac{\partial z_q^{(1)}}{\partial x_i} \\ + \frac{\partial y}{\partial z_m^{(k)}} \left[\sum_n \frac{\partial z_m^{(k)}}{\partial a_n^{(k-1)}} \frac{\partial a_n^{(k-1)}}{\partial z_n^{(k-1)}} \cdots \sum_p \frac{\partial z_r^{(3)}}{\partial a_p^{(2)}} \frac{\partial a_p^{(2)}}{\partial z_p^{(2)}} \sum_q \frac{\partial z_p^{(2)}}{\partial a_q^{(1)}} \frac{\partial a_q^{(1)}}{\partial z_q^{(1)}} \frac{\partial z_q^{(1)}}{\partial x_i} \right]'$$

References

- [1] Debogdan CE. Tensile and fatigue data for irradiated and unirradiated AISI 310 stainless steel and titanium-5 percent aluminum-2.5 percent tin: Application of the method of universal slopes. 1973.
- [2] Materna-Morris E, Möslang A, Schneider HC. Tensile and low cycle fatigue properties of EUROFER97-steel after 16.3 dpa neutron irradiation at 523, 623 and 723 K. *Journal of Nuclear Materials* 2013;442. <https://doi.org/10.1016/j.jnucmat.2013.03.038>.
- [3] Grossbeck ML, Vitek JM, Liu KC. Fatigue behavior of irradiated helium-containing ferritic steels for fusion reactor applications. *Journal of Nuclear Materials* 1986;141–143:966–72. [https://doi.org/10.1016/0022-3115\(86\)90126-1](https://doi.org/10.1016/0022-3115(86)90126-1).
- [4] Nogami S, Hasegawa A, Yamazaki M. Fatigue properties of ferritic/martensitic steel after neutron irradiation and helium implantation. *Nuclear Materials and Energy* 2020;24. <https://doi.org/10.1016/j.nme.2020.100764>.
- [5] Miwa Y, Jitsukawa S, Yonekawa M. Fatigue properties of F82H irradiated at 523 K to 3.8 dpa. *Journal of Nuclear Materials*, vol. 329–333, 2004, p. 1098–102. <https://doi.org/10.1016/j.jnucmat.2004.04.029>.
- [6] Ioka I, Yonekawa M, Miwa Y, Mimura H, Tsuji H, Hoshiya T. Effect of helium to dpa ratio on fatigue behavior of austenitic stainless steel irradiated to 2 dpa. n.d. [https://doi.org/https://doi.org/10.1016/S0022-3115\(00\)00209-9](https://doi.org/https://doi.org/10.1016/S0022-3115(00)00209-9).
- [7] Vandermeulen W, Hendrix W, Massaut V, Van De Velde J. The effect of neutron irradiation on the fatigue behaviour of AISI 316L-Results of first in-pile tests. vol. 183. 1991.
- [8] Brinkman C, Korth G, Beeston J. Influence of Irradiation on the Creep/Fatigue Behavior of Several Austenitic Stainless Steels and Incoloy 800 at 700 C. Effects of Radiation on Substructure and Mechanical Properties of Metals and Alloys, ASTM International 100 Barr Harbor Drive, PO Box C700, West Conshohocken, PA 19428-2959; 1973, p. 473–90. <https://doi.org/10.1520/STP35469S>.
- [9] Beeston J, Brinkman C. Axial Fatigue of Irradiated Stainless Steels Tested at Elevated Temperatures. Irradiation Effects on Structural Alloys for Nuclear Reactor Applications, ASTM International 100 Barr Harbor Drive, PO Box C700, West Conshohocken, PA 19428-2959; 1970, p. 419–48. <https://doi.org/10.1520/STP26641S>.

- [10] Gaganidze E, Petersen C, Aktaa J, Povstyanko A, Prokhorov V, Diegele E, et al. Low cycle fatigue properties of reduced activation ferritic/martensitic steels after high-dose neutron irradiation. *Nuclear Fusion* 2011;51. <https://doi.org/10.1088/0029-5515/51/8/083012>.
- [11] Petersen C, Povstyanko A, Prokhorov V, Fedoseev A, Makarov O, Walter M. Tensile and low cycle fatigue properties of different ferritic/martensitic steels after the fast reactor irradiation “ARBOR 1.” *Journal of Nuclear Materials* 2009;386–388:299–302. <https://doi.org/10.1016/j.jnucmat.2008.12.112>.
- [12] Gaganidze E, Petersen C. Post irradiation examination of RAF/M steels after fast reactor irradiation up to 71 dpa and < 340°C (ARBOR 2) : RAFM steels: metallurgical and mechanical characterisation. (KIT Scientific Reports ; 7596). KIT Scientific Publishing; 2011. <https://doi.org/10.5445/KSP/1000023594>.
- [13] Yang ZR, Yang Z. Artificial Neural Networks. *Comprehensive Biomedical Physics* 2014;6:1–17. <https://doi.org/10.1016/B978-0-444-53632-7.01101-1>.
- [14] Paszke A, Gross S, Massa F, Lerer A, Bradbury J, Chanan G, et al. PyTorch: An Imperative Style, High-Performance Deep Learning Library 2019.
- [15] Klambauer G, Unterthiner T, Mayr A, Hochreiter S. Self-Normalizing Neural Networks 2017.
- [16] Jiang L, Hu Y, Liu Y, Zhang X, Kang G, Kan Q. Physics-informed machine learning for low-cycle fatigue life prediction of 316 stainless steels. *Int J Fatigue* 2024;182. <https://doi.org/10.1016/j.ijfatigue.2024.108187>.
- [17] S.R. Sukhdeve. Step Up for Leadership in Enterprise Data Science and Artificial Intelligence with Big Data: Illustrations with R and Python. Independently Published; 2020.
- [18] C. Müller A, Guido S. Introduction to Machine Learning with Python, A Guide for Data Scientists. O’Reilly Media Inc.; 2016.
- [19] Lundberg S, Lee S-I. A Unified Approach to Interpreting Model Predictions 2017.
- [20] Rahat A, Wood M. On Bayesian Search for the Feasible Space Under Computationally Expensive Constraints 2020.